Materials Science & Engineering R 163 (2025) 100929

Contents lists available at ScienceDirect

Materials Science & Engineering R

journal homepage: www.elsevier.com/locate/mser

Galvanic cell metasurface modulating electron transfer on polymer implants for sterilization and osteointegration

Shiwei Guan [a,1], Zhiyu Hou [a,1], Xianming Zhang [a], Yuanming Cao [b], Shi Qian [a], Xingdan Liu [a], Fang Wang [a], Hongqin Zhu [a], Dandan Li [a], Paul K. Chu [d], Ji Tan [a,*], Xuanyong Liu [a,b,c,**]

[a] State Key Laboratory of Advanced Ceramics, Shanghai Institute of Ceramics, Chinese Academy of Sciences, Shanghai 200050, China
[b] College of Biological Science and Medical Engineering, Donghua University, Shanghai 201620, China
[c] School of Chemistry and Materials Science, Hangzhou Institute for Advanced Study, University of Chinese Academy of Sciences, 1 Sub-lane Xiangshan, Hangzhou 310024, China
[d] Department of Physics, Department of Materials Science & Engineering, and Department of Biomedical Engineering, City University of Hong Kong, Tat Chee Avenue, Kowloon, Hong Kong

ARTICLE INFO

Keywords:
Polymer implant
Bimetallic
Galvanic cell metasurface
Antibacterial
Osseointegration

ABSTRACT

Bacterial infections challenge clinical medicine, and "electrostimulation" and "catalytic therapy" offer novel antibacterial strategies beyond antibiotics and metal ions. Herein, a bimetallic galvanic cell metasurface composed of biosafe zirconium (Zr), titanium (Ti), and tantalum (Ta) is fabricated on polymer implants using a developed plasma modification system (PIII&PHS). The galvanic cell metasurface harbors an asymmetric charge to modulate electron transfer, and enables "electron beam flow" to surpass the reactivity limits of metals. Remarkably, the galvanic cell metasurface adeptly modulates electron transfer to reduce the energy supply and triggers the bacterial reactive oxygen species (ROS) imbalance to cause death. The antibacterial mechanism is validated, and the universality is demonstrated. Rat osteomyelitis, cranial defect, and rabbit femoral defect models corroborate the excellent osteointegration ability of the galvanic cell metasurface. The results reveal that incorporating biosafe bimetallic asymmetric charges into a metasurface is a novel and effective strategy for designing antibacterial medical materials.

1. Introduction

Bacterial infections on medical implants delay patient recovery and increase morbidity [1,2]. The ideal implantable devices should have antibacterial and tissue-repairing capabilities [3–6]. There is an urgent need to develop a safe strategy to prevent bacterial infections and promote tissue regeneration [7–9]. Bacteria are prokaryotes without specific energy-supplying mitochondria. Extramembrane electron transfer is crucial to bacterial energy metabolism [10,11], because disruption of electron transfer disturbs the balance of bacterial ROS homeostasis and damages bacterial vital biomolecules [12,13]. In addition, during bacterial respiration, electrons are transferred to extracellular acceptors *via* outer membrane c-cytochromes and conductive pili [14,15]. In this respect, galvanic cells with electronic interference functions constitute a novel strategy for antibacterial applications [13]. Our previous work demonstrates that metal-mediated microcouples can consume protons in the outer membrane, cut off the bacterial ATP supply, and kill bacteria [16]. In addition, surface charges can disrupt the bacterial membrane potential and cause irreversible damage to the membrane structure [17,18].

Traditionally, metal antibacterial action primarily relies on metal ions such as Zn, Cu, Ga, and Ag ions [19,20]. These ions have demonstrated effective performance in eliminating pathogens, thereby alleviating the problem of antibiotic resistance to a certain extent. However, potential toxicological issues cannot be ignored. Biosafe metals such as Zr, Ti, and Ta are commonly used in clinical implants due to their long-term safety [6]. "Asymmetric charge" refers to a situation where the distribution of charge is not evenly balanced or symmetrical. Charge distribution in metals is primarily due to free electrons. The electrons can move freely within the metal, forming an "electron cloud". Different

* Corresponding author.
** Corresponding author at: State Key Laboratory of Advanced Ceramics, Shanghai Institute of Ceramics, Chinese Academy of Sciences, Shanghai 200050, China.
E-mail addresses: tanji@mail.sic.ac.cn (J. Tan), xyliu@mail.sic.ac.cn (X. Liu).
[1] Co-first author

https://doi.org/10.1016/j.mser.2025.100929
Received 16 October 2024; Received in revised form 22 December 2024; Accepted 5 January 2025
Available online 18 January 2025

metal surfaces have different surface charge distributions. Constructing asymmetric charge-distribution structures to achieve an electrical effect on antibacteria is possible in Zr, Ti, and Ta. However, as favored clinical implant materials, Zr, Ti, and Ta lack antibacterial and osteogenic activities. Researchers have been dedicated to developing antibacterial properties in metals such as Zr, Ti, and Ta [21–24]. Asymmetric design plays a unique role in materials construction [25,26]. For example, Wu et al. have designed an asymmetric magnesium/molybdenum bimetallic microelectrode that can continuously release 1 V direct current to stimulate intestinal tissues and promote extracellular secretion of healing factors [27]. Additionally, the concept of a metasurface has attracted research interest [28]. A metasurface is an artificial sheet material with sub-wavelength, two-dimensional structures engineered to manipulate electromagnetic waves, even electrons. The metasurface can manipulate the wavefront of the light by locally controlling its phase, amplitude, and polarization. Just as metasurfaces can manipulate photons, they can also potentially control electrons. Actually, the metasurface potentially subverts the potential distribution determined by the inherent properties and arrangements of microscopic particles in the materials, consequently fostering the physical regulation of electron transport. Therefore, combining bimetallic galvanic cells with a metasurface can enhance the metal catalytic activity.

Polymer materials such as polyetheretherketone (PEEK), polyetherketone (PEKK), and polyarylsulfone (PASF) have good biocompatibility and chemical stability and do not dissolve or leach harmful materials in the body [29]. PEEK was approved for use in humans by the Food and Drug Administration in 1998 and is widely used in orthopedics and craniofacial surgery [30]. However, bacterial infections triggered by the lack of antibacterial activity can cause implant failure. Therefore, it is crucial to endow PEEK and other polymer implants with antibacterial properties and promote tissue repair [31,32]. However, the significant chemical inertness of polymers presents challenges to surface activation. Although it is common practice to employ concentrated sulfuric acid to modify the surface [33]. There are still no antibacterial polymer implants with real clinical applications. The challenge is to consider the sometimes conflicting issues of antibacterial function and biosafety.

In this work, a bimetallic galvanic cell metasurface (GCMS) is fabricated on seven types of polymers by plasma immersion ion implantation (PIII) and plasma homopolar sputtering (PHS) modification (Fig. 1). PIII and PHS were integrated into plasma system (PIII&PHS), effectively improving production efficiency and yield. The metasurface design overcomes the challenge of low electroactivity in bimetallic galvanic cells and regulates electron transport. The GCMS exhibits broad-spectrum sterilization by interfering with bacterial metabolism and ROS balance through electron cycling. Meanwhile, the surface

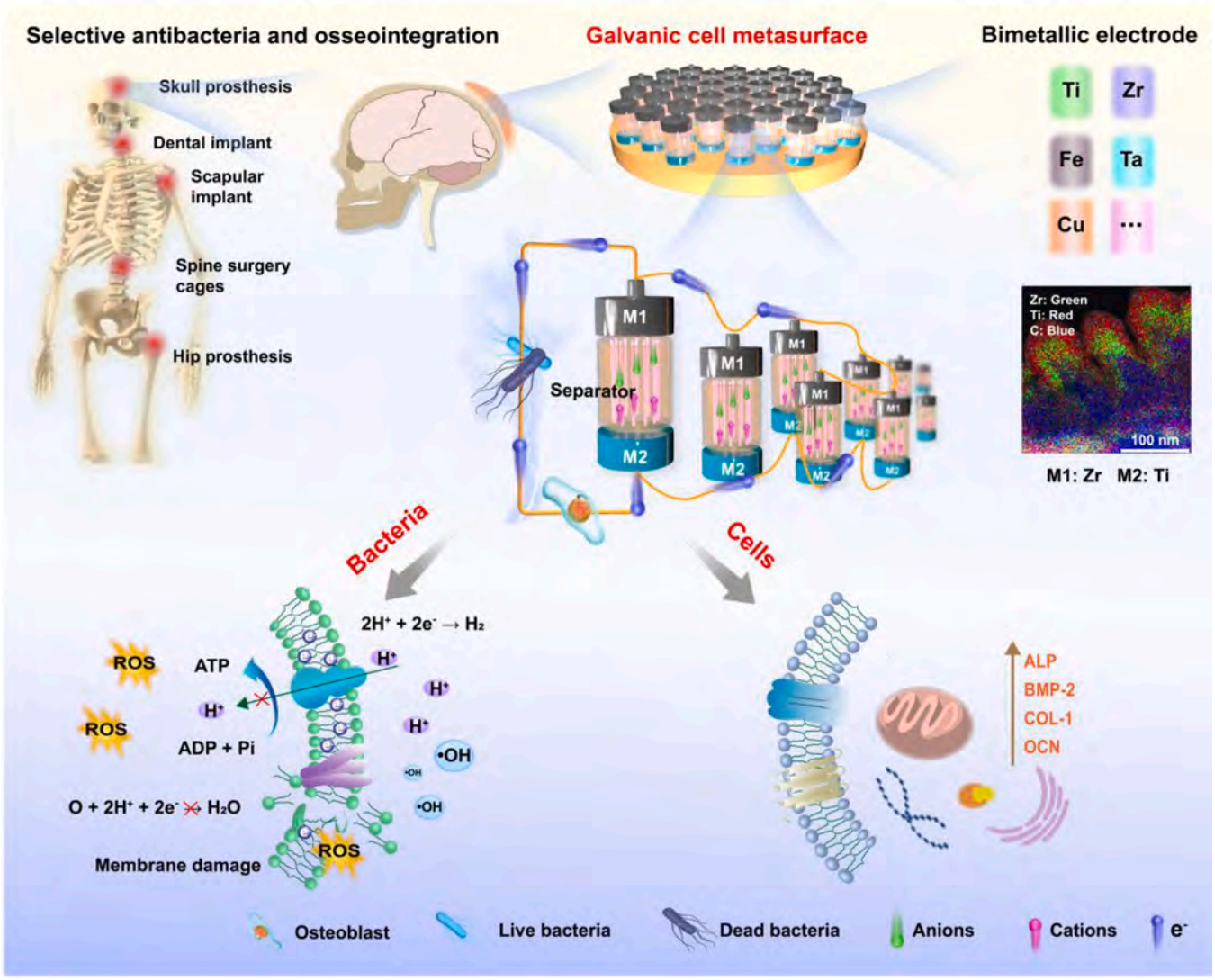

Fig. 1. Schematic diagram of GCMS for sterilization and bone repair. The PIII&PHS technique is developed to construct nanopillar array films on PEEK. The nanopillar arrays exhibit parallel galvanic cell properties to effectively electroshock sterilization and induce osseointegration.

electroactive microenvironment positively regulates bone tissues [34, 35]. Bone defect models of rats and rabbits and femoral defect models highlight the clinical translation potential of the Zr/Ti bimetallic GCMS. The antibacterial mechanism of the GCMS is validated using various randomized bimetallic combinations, including Ti, Zr, Ta, Fe, and Cu, to demonstrate the universality.

2. Results and discussion

2.1. Construction of galvanic cell metasurface

Vacuum ion coating is a complex process that combines arc discharge, ion sputtering, ion deposition, and ion implantation. The PIII process is often plagued by sputtering of contaminants in the vacuum chamber, such as the sample holder, and shielding is frequently implemented to mitigate secondary deposition [36]. Here, an alternative approach is adopted by harnessing the capabilities of ion sputtering deposition while applying a homopolar bias to the target containing the element to be introduced, resulting in the PHS technology (Fig. 2A). It's important to highlight that, in terms of surface modification principles, PIII and PHS are classified as two distinct technologies: ion implantation and sputtering deposition, respectively. In this study, PHS was combined with PIII to form the PIII&PHS modification system, in which energetic Ar^+ bombardment was used to attain film growth and etching in a dynamic equilibrium. This is suitable for semi-crystalline polymers such as PEEK, PEKK, PASF, polyamide-imide (PAI), polyetherimide (PEI),

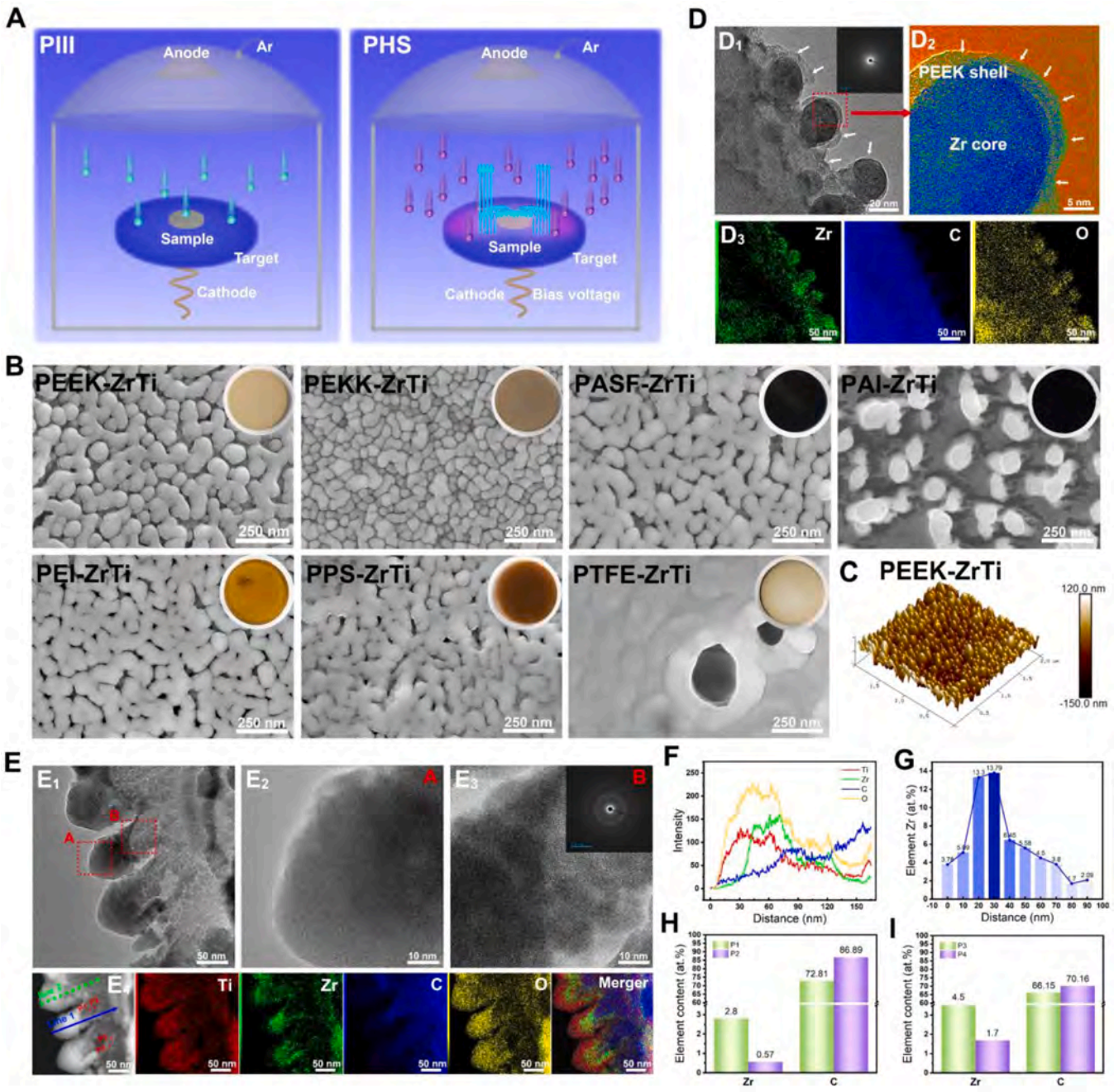

Fig. 2. PIII&PHS modification system and characterization of GCMS. (A) Schematic diagram of the PIII&PHS system. (B) SEM images of PEEK-ZrTi, PEKK-ZrTi, PASF-ZrTi, PAI-ZrTi, PEI-ZrTi, PPS-ZrTi, and PTFE-ZrTi. The images inset in the upper right are photographs of the sample. (C) AFM image of PEEK-ZrTi surface topography. HRTEM images, SAED patterns, and mapping of PEEK-Zr (D), and PEEK-ZrTi (E). Line scan image of area line 1 (F) and line 2 (G). (H, I) Element content of point 1, point 2, point 3, and point 4.

polyphenylsulfide (PPS), and polytetrafluoroethylene (PTFE) for the construction of a metasurface with a nanopillar array (Fig. 2B, Fig. S1) confirmed by both AFM conducted on PEEK-ZrTi and SEM. The nanopillars with heights of 50–150 nm are distributed uniformly on the substrate surface (Fig. 2C). In the future, PIII&PBH may promote the structure-function integrated modification in flexible fibers and 3D-printed polymers.

The transmission electron microscopy (TEM) image of PEEK-Zr reveals a nanospherical surface structure with a 1–3 nm thick PEEK shell around the core (Fig. 2D), confirming that Zr ions are injected into the PEEK substrate to form the core-shell structure of PEEK-coated Zr nanoclusters (Fig. 2D). After the deposition of Ti films on the PEEK-Zr surface by PHS, PEEK-ZrTi has a nanopillar array structure (Fig. 2-E_1, Fig. S2). The Ti layer has a dense structure (Fig. 2-E_2) with a thickness of about 50 nm, while the Zr layer consists of a stack of irregular nanoclusters (Fig. 2-E_3). The inner part of the nanopillar array has a "lattice structure", and the "gap" between the Zr nanopillars is the PEEK substrate (Fig. 2-E_3). The compositional distribution of PEEK-ZrTi clearly distinguishes the Ti layer outside the nanopillar from the Zr layer inside (Fig. 2-E_4, Fig. S3, Fig. S4). Selected-area electron diffraction (SAED) shows that PEEK-ZrTi has an amorphous structure (Fig. 2-E_3). Ti is distributed in the outer layer at 60 nm, while Zr is distributed at 20–70 nm in the nanopillar (Fig. 2F, Fig. 2G). C is found throughout the nanopillar, and its concentration increases gradually from the outside to the inside. Positions P1-P4 inside the nanopillar are analyzed for Zr and C. The dark areas in the HR-TEM image are the Zr clusters, in which the C content is smaller. The "gap" between Zr clusters is dominated by C (Fig. 2H), suggesting Zr is present as nanoclusters in the nanopillar and PEEK around the clusters. The results of between different nanocolumns support the assessment (Fig. 2I).

2.2. Characterization and growth mechanism

The survey XPS spectra of PEEK, PEEK-Zr, PEEK-Ti, and PEEK-ZrTi are shown in Fig. S5A. PEEK-ZrTi shows characteristic peaks of C, O, Ti, and Zr. The Ti 2*p* (Fig. S5B) and Zr 3*d* (Fig. S5C) peaks correspond to TiO_2 and ZrO_2, respectively. Surface oxidation plays an important role in surface passivation and protection. The high-resolution spectra of C 1 *s* indicate that carbonization occurs (Fig. S5D). XPS depth profiling shows that PEEK-ZrTi contains Ti and Zr (Fig. 3A, B), with Ti distributed in the outer layer of the galvanic cell and Zr in the inner layer. It was due to the high-energy injection of Zr^{4+} into PEEK during PIII and the low-energy deposition of Ti by PHS (Fig. 3A, B, Fig. S6A). The C concentration decreases initially and then increases, and the depth profile overlaps that of Zr from 40 to 240 nm (Fig. S6B).

Although there are apparent nanopillar arrays on PEEK-Zr and PEEK-Ti, PEEK and PEEK-Ar are relatively flat (Fig. S7). AFM and SEM produce similar results (Fig. S8A-C). The nanopillar heights show the order of PEEK-Zr > PEEK-ZrTi > PEEK-Ti (Fig. S8D). In addition, after metallization of the PEEK surface, the friction, wear properties (Fig. S9), and elastic modulus (Fig. 3C) improve. The nanopillar structure increases the surface roughness (Fig. S10) and friction coefficient (Fig. S11), boding well for mechanical durability. Ion release was determined by inductively coupled plasma mass spectrometry (ICP-MS, Fig. S12), Zr^{4+} release from PEEK-Zr was higher than that from PEEK-ZrTi in the Tris-HCl buffer solution. Ti^{4+} release from PEEK-Ti was 0.081 μg mL^{-1} at 28 days. However, the Ti^{4+} release of PEEK-ZrTi was only 0.001 μg mL^{-1}, which may be below the detection limit. The results indicate that the PHS-deposited Ti films have strong binding and mechanical stability. The result is beneficial for the completion of the film during the bone implantation process.

A good understanding of the growth mechanism of GCMS is important. As shown in Fig. 3D, the polymers are mostly semi-crystalline with amorphous regions (i) [37]. The molecular chains in the amorphous regions are broken during the Ar-PIII process, forming the carbon-weak areas of Polymer-Ar (ii). In the M1-PIII process, $M1^{x+}$ is injected into the substrate, forming M1 nanoclusters surrounded by an insulating polymer layer. The weak areas of Polymer-M1 are bombarded and depressed, with crystalline regions remaining to form columnar protrusions (iii). In the M2-PHS process, the M2 target is sputtered by Ar^+ and deposited onto the M1 nanoclusters under a bias voltage to form the Polymer-M1M2 nanopillar metasurface (iv). As shown in Fig. 3D (v), polymer samples are insulating and exhibit capacitive properties, which consume some of the bias potential. During the PHS process, ions are deposited onto the sample at the bias voltage to form films with superior mechanical properties compared to those produced by traditional magnetron sputtering [38].

There are two processes in the plasma sheath, one in which the target element is deposited onto the sample surface, the other in which the film is deposited is re-sputtered from the sample:

$$Q_s = AC\gamma(j_{iT} - j_{iS}), \tag{1}$$

where Q_s is the deposition rate of the sample surface, j_{iS} and j_{iT} represent the densities of ion flow of the sample and target, respectively, and A and C are constants. The polymer substrate is an insulator and accumulates a large amount of charge. At the beginning, $j_{iS} \approx 0$ so Q_s is maximum. As the metal is deposited on the surface, the surface conductivity of the substrate increases. Therefore, the bias potential V_s decreases, and $j_{iT} > j_{iS}$ decreases Q_s. As deposition continues in PHS, $j_{iT} = j_{iS}$. At this point, $Q_s = 0$, and metal deposition reaches a dynamic equilibrium versus sputtering on the sample surface.

As shown in Fig. 3D (v), the gap in the metasurface nanopillar array resembles a nanotube-like structure with a diameter, d. Q_s at the inner wall of the nanotube is hindered by the potential drop $\Delta\varphi$ of pores [39, 40]. $\Delta\varphi$ can be calculated by:

$$\Delta\varphi = ((d/2)/D_d)^2\varphi, \tag{2}$$

where D_d is the critical value of the spacing distance, and $\Delta\varphi$ in the pores implies that the plasma accumulates below the surface of the columnar protrusions of Polymer-M1. Consequently, the columnar protrusions become sites for selective deposition. Nanopillars are grown dynamically to form a metasurface with a nanopillar spacing of $d/2 < D_d$. The unique advantages of PIII&PHS bode well for the fabrication of the GCMS. For a complete description, please refer to the supplementary information "Metasurface growth mechanism."

Different metals have different charge distributions. The potential difference formed by the asymmetric charge of the bimetal is the driving force of the galvanic cell. The potentials of Meta-Zr, Meta-Ti, and Meta-Ta are −64.60 mV, −55.22 mV, and −48.01 mV, respectively, at a pH of 7.4 (Fig. 3E). The bacterial environment is usually weakly acidic (about 6.0–6.5). The potentials of Meta-Zr, Meta-Ti, and Meta-Ta are −57.15 mV, −41.44 mV, and −39.41 mV, respectively, at a pH of 6.5 (Fig. 3E). There is a significant difference between the plane and metasurface potentials composed of Zr, Ti, and Ta, suggesting that the metasurface can modulate the metal electrode potential (Fig. S13). The potential of a bimetallic galvanic cell determines the efficiency of electron transfer. The greater the difference in the electrode potential of the two metals, the higher the efficiency of electron transfer and the higher the surface electroactivity. Here, "electroactivity" refers to the surface electron transfer driven by the asymmetric potential. In a bimetallic galvanic cell, electrons always flow from the metal with a lower potential to the metal with a higher potential, and this flow of electrons forms a current. Electrical tests show that the surface of PEEK-ZrTi exhibits a short-range current (Fig. 3F), with corresponding increases in electric signals at the nanoscale regions (Fig. S14). Still, no long-range conductivity is observed (Fig. S15). The galvanic cells generate electrical signals, suggesting that the bimetallic GCMS shows a microregional electrical effect. The TMB color development reaction demonstrated that GCMS can electro-catalytically produce ROS. The electrocatalytic hydroxyl radical (•OH) oxidizes the colorless TMB to blue ox-TMB with a significant enhancement in the absorbance

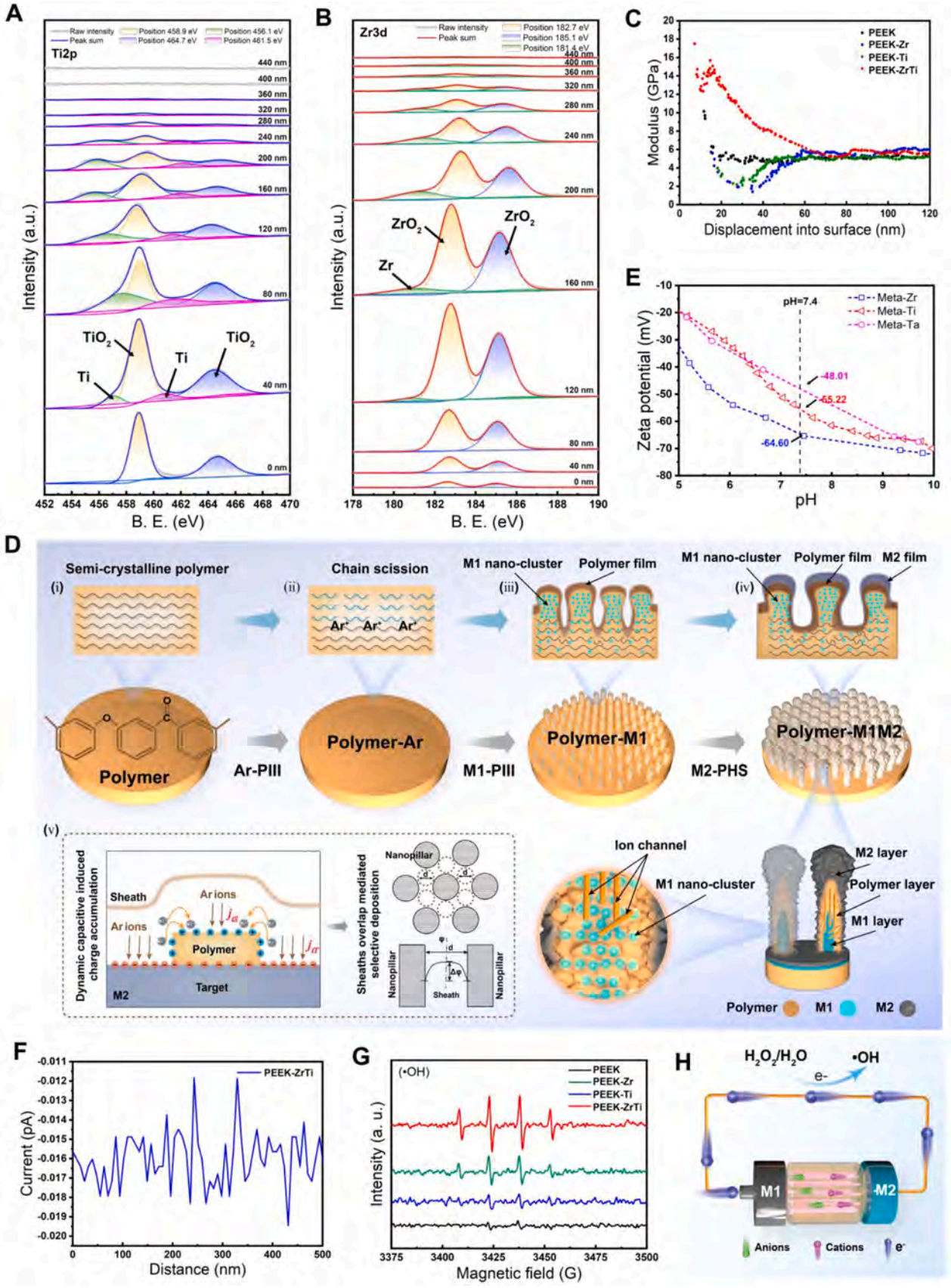

Fig. 3. Characterization and growth mechanism of GCMS. (A) Ti 2*p* and (B) Zr 3*d* XPS spectra at various depths. (C) Nanoelastic modulus of various samples. (D) Schematic diagrams of the mechanisms of the GCMS. (E) Surface Zeta potential of Meta-Zr, Meta-Ti, and Meta-Ta (Meta means metasurface on substrate). Mono-metallic metasurfaces constructed using Ar gas assistance. (F) Surface currents of PEEK-ZrTi measured using the four-probe method. (G) EPR spectra demonstrating the •OH generation of various samples. (H) Diagram of electrocatalysis for GCMS.

(Fig. S16), demonstrating that GCMS electro-catalytically produces ROS. EPR shows that the Zr/Ti bimetallic galvanic cell catalyzes the production of •OH from H_2O_2 or H_2O (Fig. 3G). The GCMS shows one type of Fenton-like reaction produced by electrons (Fig. 3H) [41]

2.3. Antibacterial properties of galvanic cell metasurface

Fig. 4A illustrates the antibacterial assessment of GCMS, revealing outstanding antibacterial performance for PEEK-ZrTi, PEKK-ZrTi, PASF-ZrTi, PAI-ZrTi, PEI-ZrTi, and, PPS-ZrTi. The PEEK-ZrTi, PEKK-ZrTi, and PASF-ZrTi plates revealed minimal numbers of bacteria. Compared to PEEK, PEEK-Zr and PEEK-Ti do not show antibacterial effects, suggesting that monometallic nanofilms lacked bactericidal properties (Fig. S17). The hardness and melting points of various polymer implants differ, leading to variations in their surface structures, and consequently, their antibacterial capabilities. Of these, the PTFE-ZrTi metasurface is the least pronounced, with its antibacterial ability lagging behind other polymer implants. The morphology of *Staphylococcus aureus* (*S. aureus*) and *Escherichia coli* (*E. coli*) on the unmodified substrate is intact, but *S. aureus* (Fig. 4B) and *E. coli* (Fig. 4C) on the GCMS leak many intracellular contents. The antibacterial performance shows that the GCMS possesses a broad-spectrum antibacterial resistance with an antibacterial rate of 99.99 % (Fig. 4D, E).

To further reveal the electron transfer mechanism of the GCMS, we explore the effects of bipolar metal potential, polymer diaphragm, and metasurface parameters on the antibacterial performance. In the bimetallic electrodes (Fig. 4F), the two poles of the electrodes are constructed with the same Zr to form a PEEK-ZrZr metasurface. The loss of antibacterial properties in PEEK-ZrZr demonstrates that the bimetallic electrode potential is essential for providing antibacterial characteristics

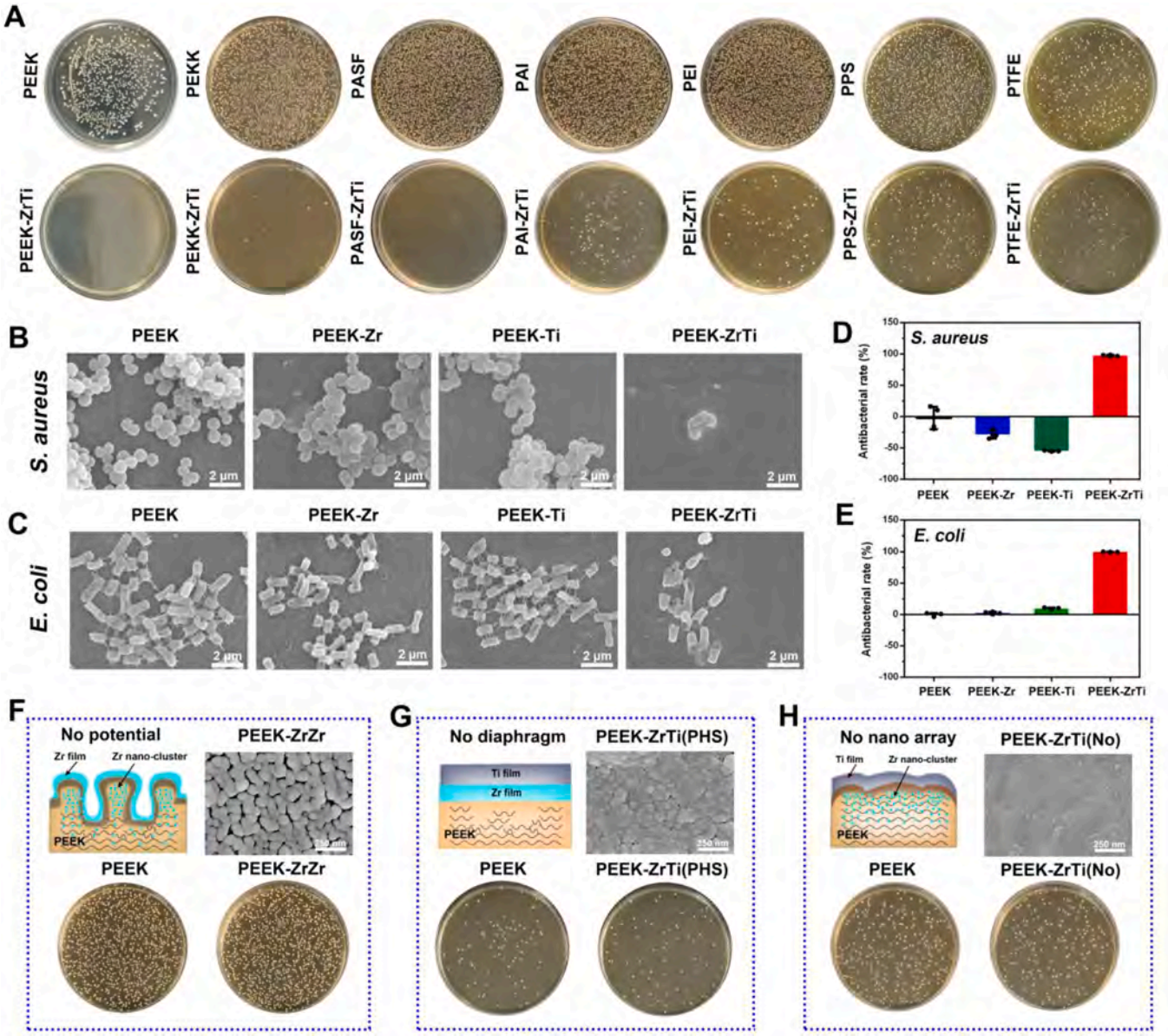

Fig. 4. Antibacterial properties of the galvanic cells metasurface. (A) The photographs of *S. aureus* colonies for PEEK-ZrTi, PEKK-ZrTi, PASF-ZrTi, PAI-ZrTi, PEI-ZrTi, PPS-ZrTi, and PTFE-ZrTi GCMS. SEM images of the (B) *S. aureus* and (C) *E. coli* with various samples. The corresponding antibacterial efficiency of different groups for (D) *S. aureus* and (E) *E. coli*. (F) The photographs of colonies and SEM images of PEEK-ZrZr. Homogeneous Zr metals were used to construct potential-free array films, i.e., Zr-PIII composite Zr-PHS. (G) The photographs of colonies and SEM images of PEEK-ZrTi(PHS). Diaphragm-free bimetallic deposition of metasurface. i.e., Zr-PHS composite Ti-PHS. (H) The photographs of colonies and SEM images of PEEK-ZrTi(No). A bimetallic film without metasurface. i.e., PEEK-ZrTi was prepared without the Ar-PIII step.

to the galvanic cell. As for the polymer diaphragm (Fig. 4 G), by replacing Zr-PIII with Ti-PHS, the loss of the injection depth of Zr^{4+} leads to the disappearance of the galvanic cell diaphragm, resulting in a direct contact between Zr and Ti. The PEEK-ZrTi (PHS) metal electrode is short-circuited, thereby eliminating the antibacterial properties. About the metasurface, the biosafe bimetallic Ti, Zr, and Ta show a limited potential difference, but the design of the metasurface makes it possible to amplify the difference (Fig. 4H). The metasurface exhibits an "electron beam flow" amplification effect through the parallel connection of multiple galvanic cells. The concept of "electron flow" has a rich historical background and is extensively utilized in various industrial processes such as metal forming manufacturing, welding, and coating

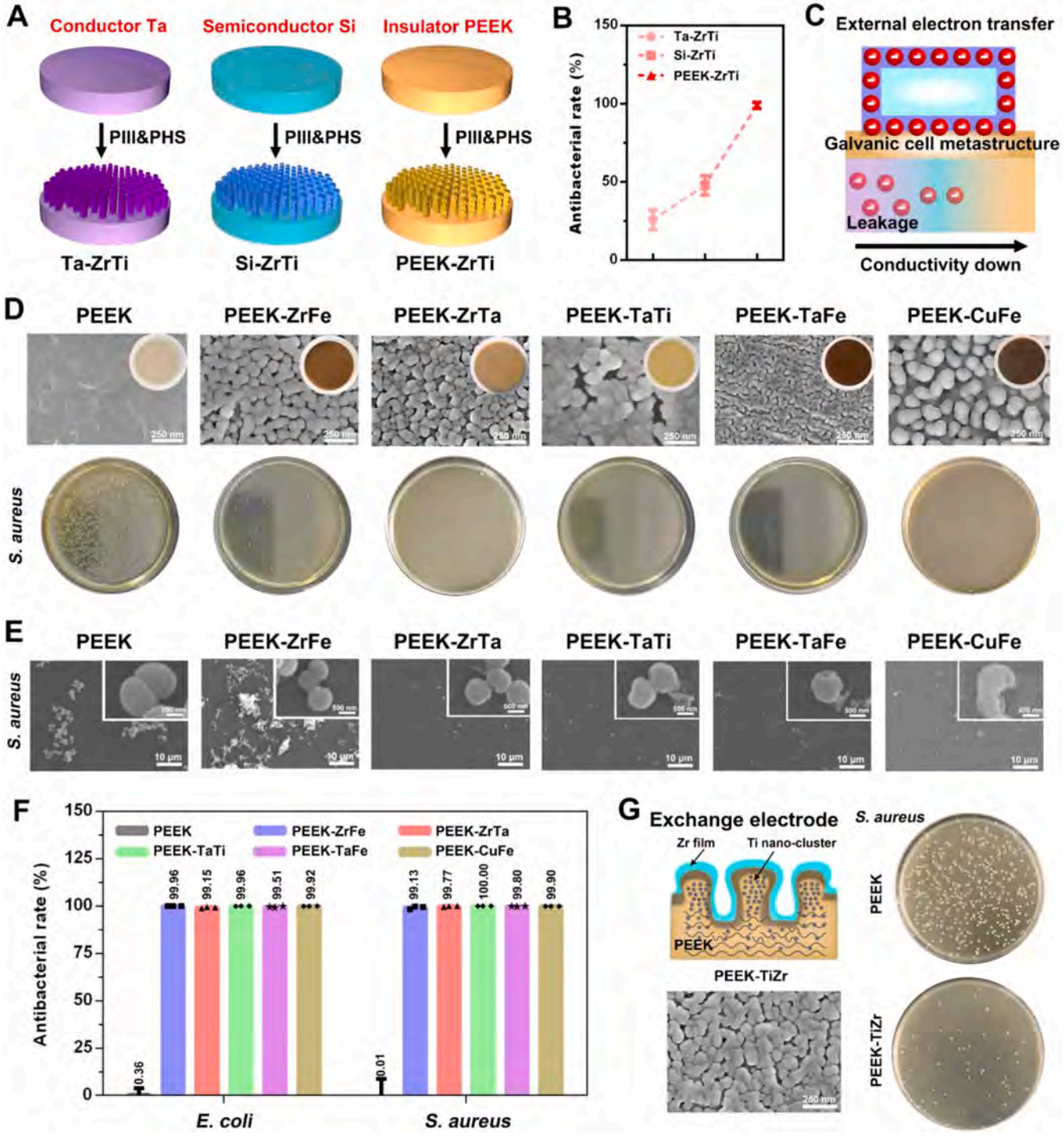

Fig. 5. Characterization and antimicrobial universality of galvanic cells metasurface. (A) Schematic illustration for the fabrication of the testing Zr/Ti bimetallic film, i.e., Zr/Ti bimetallic galvanic cell films on conductor Ta (Ta-ZrTi), semiconductor Si (Si-ZrTi), and insulator PEEK substrates (PEEK-ZrTi). (B) Antibacterial rates of Ta-ZrTi, Si-ZrTi, and PEEK-ZrTi. (C) Schematic illustration of electron transfer for the bimetallic galvanic cells. (D) SEM images and photographs of *S. aureus* colonies of the GCMS with different bimetallics. (E) Random combinations of biosafety metals such as Ti, Zr, Ta, Fe, and Cu were utilized. Exploration of the generalization of PIII&PHS bimetallic galvanic cells. (F) The corresponding antibacterial efficiency of different bimetallic galvanic cells. (G) PEEK-TiZr galvanic cell array films were constructed by first Ti-PIII and then Zr-PHS.

preparation. Electrons are propelled toward an anode due to the electric field established by the voltage difference between the cathode and anode [42,43]. We referred to the concept of "electron beam" and defined it as the "electron beam flow" effect based on the metasurface characteristics. The metasurface is structured as an array of nanopillars, each functioning as a bimetallic galvanic cell with a defined potential distribution. This structure facilitates unidirectional electron movement within each nanopillar. Consequently, the array of nanopillars operates akin to a parallel grouping of galvanic cells, thereby enhancing the current. Analogous to a light beam composed of photons traveling coherently in one direction, an electron beam flow comprises a stream of electrons moving uniformly toward a specific direction. Without the metasurface, the PEEK-ZrTi (No) bimetallic galvanic cell loses its efficient electrocatalytic activity and cannot kill bacteria effectively. The application of metasurface regulation of electroactive mechanisms in antibacterial applications is the focus of this article. Metasurface may have important implications in surface sensing and electro-catalysis fields.

The electron transfer process is noticeably affected by the conductivity of the substrate. Especially, for two-dimensional structures like metasurfaces, the effect of electron transfer at the interface between the surface and the substrate is more pronounced. Different conductivity substrates such as Ta, silicon (Si), and PEEK are selected to construct the Ta-ZrTi, Si-ZrTi, and PEEK-ZrTi galvanic cell films shown in Fig. 5A. The

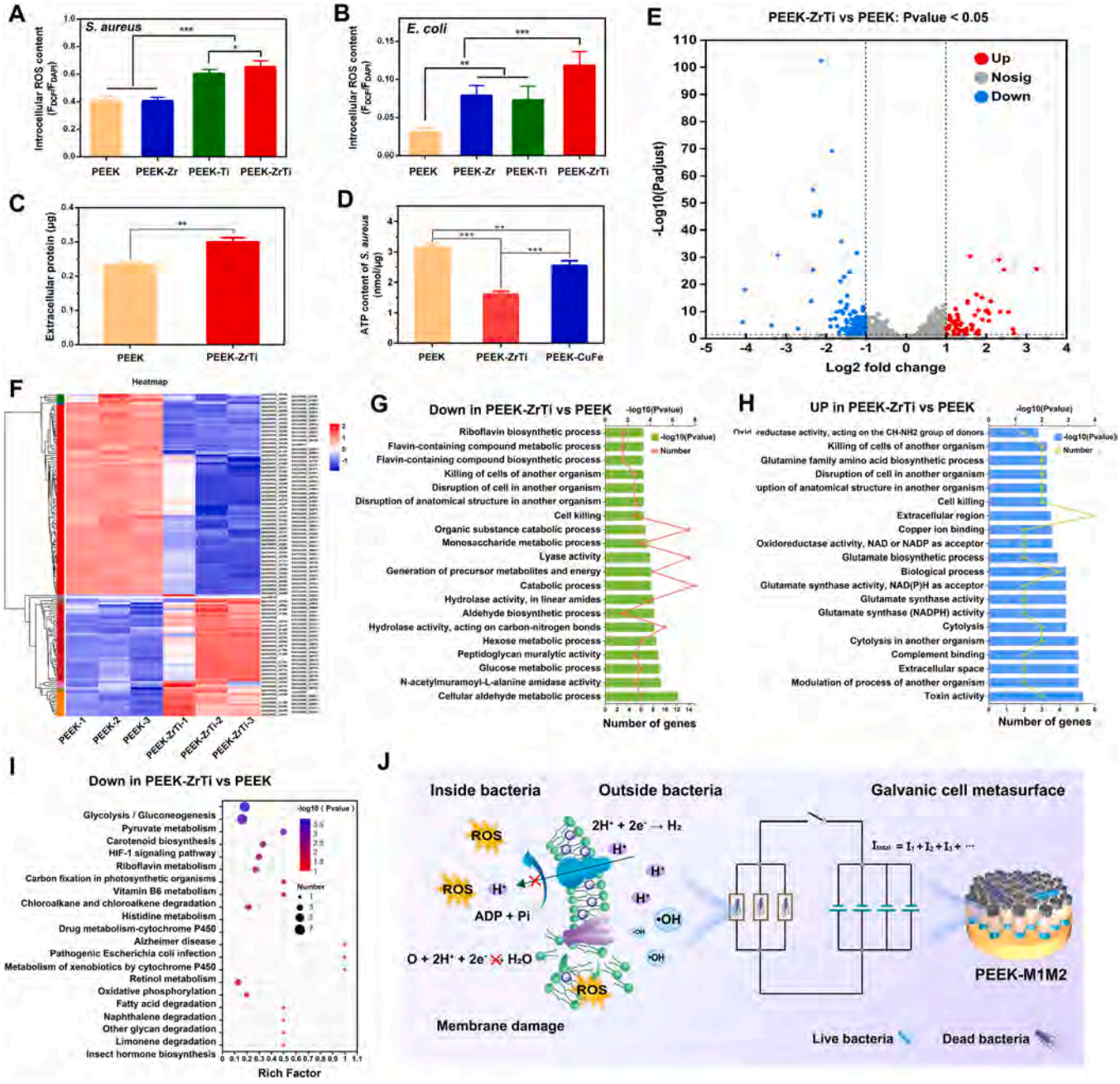

Fig. 6. Antibacterial mechanism of the galvanic cells metasurface. ROS levels of (A) *S. aureus* and (B) *E. coli.* (C) Extracellular protein and (D) ATP content of *S. aureus* for various samples. (E) Volcano plot of transcriptomic analysis of differentially expressed genes. n = 3 independent experiments per group. (F) Heatmap analysis of differentially expressed genes. The range from −1 to + 2 indicates the relative gene expression of PEEK-ZrTi vs control PEEK. (G) Down-regulated and (H) up-regulated gene ontology (GO) enrichment analysis in PEEK-ZrTi compared with PEEK. (I) Downregulated enriched Kyoto Encyclopedia of Genes and Genomes (KEGG) pathways analysis in PEEK-ZrTi compared with PEEK. (J) Schematic diagram of the antibacterial mechanism of the GCMS.

antibacterial rates of Ta-ZrTi, Si-ZrTi, and PEEK-ZrTi increase gradually and are negatively correlated with substrate conductivity (Fig. 5B, Fig. S18). The lower the substrate conductivity, the less electron transfer occurs at the interface between the GCMS and the substrate. More electrons flow unidirectionally to the outer surface to enhance the catalytic effect (Fig. 5C) [5]. This result further verifies the electrocatalytic mechanism of the galvanic cell.

To investigate the universality of PIII&PHS and practical viability, five metals (M: Ti, Zr, Ta, Fe, and Cu) are selected to construct the bimetallic GCMS. As shown in Fig. 5D, the nanopillar metasurface was formed on PEEK-M1M2. Despite certain differences due to varying ionization rates and sputtering rates of different metals, all the samples exhibited significant antibacterial effects. The dead *S. aureus* cells are shriveled and wrinkled (Fig. 5E). The corresponding *E. coli* bactericidal effect is consistent with that of *S. aureus* (Fig. S19). The antibacterial rates of PEEK-ZrFe, PEEK-ZrTa, PEEK-TaTi, PEEK-TaFe, and PEEK-CuFe are over 99.13 % for *E. coli* and *S. aureus*, respectively (Fig. 5F). The positive and negative electrodes of the exchanged galvanic cells are tested for antibacterial properties. The results demonstrate that the GCMS, with the exchange of bimetal internal and external orders, retains the antibacterial action (Fig. 5G). Therefore, the antibacterial mechanism of the bimetallic GCMS based on PIII&PHS is universal, which is difficult to achieve with existing technologies and has not been reported.

2.4. Osteomyelitis model to assess antibacterial resistance

ROS are common signaling molecules in cells, primarily produced by the respiratory chain, that stably transfer electrons to O_2. Changes in ROS production rates during oxidative stress lead to elevated levels of intracellular ROS, which can be lethal to bacteria [44]. Bacteria cultured on GCMS show significantly elevated intracellular ROS for *S. aureus* (Fig. 6A) and *E. coli* (Fig. 6B), disruption of bacterial bacteriophage membranes, and leakage of large amounts of intracellular proteins (Fig. 6C). In addition, the galvanic cell effect disrupts the bacterial energy transfer chain and the blockage of ATP synthesis (Fig. 6D).

To further explore the antibacterial mechanism, whole transcriptome RNA sequencing is performed. There are 20.56 and 20.82 million clean reads for PEEK and PEEK-ZrTi, respectively, and 94.82 % and 94.90 % of clean reads are mapped, respectively (Table S1). There are 59 up-regulated and 100 down-regulated genes in PEEK-ZrTi compared to the PEEK group, indicating the relatively high cellular response of the PEEK-ZrTi group (Fig. 6E). The related gene expression of signaling pathways is shown in Fig. 4F. There are significant differences in PEEK and PEEK-ZrTi. Subsequently, a Gene Ontology (GO) enrichment analysis is carried out. Fig. 6G and H illustrate that the down-regulated genes are primarily concentrated in the energy metabolic process (hexose metabolic process, peptidoglycan muralytic activity, glucose metabolic process, organic substance catabolic process, and monosaccharide metabolic process). In contrast, up-regulated genes are mainly enriched in the enzymatic activity (glutamate synthase activity, NAD(P)H as acceptor, glutamate synthase activity, glutamate synthase (NADPH) activity, glutamate synthase activity, NAD(P)H as acceptor, oxidoreductase activity, acting on the CH-NH2 group of donors). *S. aureus* infection, mineral absorption, nitrogen metabolism, and so on were up-regulated (Fig. S20), while glycolysis/Gluconeogenesis, pyruvate metabolism, carotenoid biosynthesis, and so on were down-regulated (Fig. 6I). The related gene expression of the above signaling pathways is shown in Fig. S21. The antibacterial mechanism is shown in Fig. 6J, in which the GCMS consists of parallel galvanic cell units, current satisfies I total = I1 + I2 + I3 + •••. Cells are connected in parallel to enhance the current by utilizing the "electron beam flow" effect. The external circuit creates a microenvironment for electrocatalytic ROS activation, which disrupts the bacteria's intra/extracellular redox balance. Bacteria complete aerobic respiration through electron transfer across the cell membrane, which transfers electrons to oxygen through some membrane-bound proteins [14,45,46]. The potential difference of surface disrupts bacterial extramembrane electron transfer, enabling direct electron exchange with the adherent bacterium. This interruption blocks proton translocation and halts ATP synthesis in the bacteria. Electron transfer has the potential to deplete protons in the outer membrane, leading to the disruption of the ATP supply in bacteria, and effectively causing bacterial death. As such, surface charges can disrupt bacterial membrane potential, inflicting irreversible damage to the membrane structure.

The Zr/Ti bimetallic galvanic cells and PEEK are selected for animal trials (Fig. 7A). Just two days post-implantation, *S. aureus* colonies were nearly absent from the Zr/Ti bimetallic galvanic cell surface (Fig. 7B), in stark contrast to the abundant colonies of other surfaces. The antibacterial rate of PEEK-ZrTi GCMS is 98.35 % (Fig. 7C). Giemsa staining reveals the absence of infected tissue in the PEEK-ZrTi group (Fig. 7D), and infiltrated bacteria are observed from the remaining groups (yellow arrows). Hematoxylin-eosin (HE) staining further confirms the absence of significant inflammatory infiltration around the PEEK-ZrTi implant (Fig. 7E). Micro-CT reconstruction modeling visualizes the considerable benefit of PEEK-ZrTi in improving the infection microenvironment to promote new bone generation (Fig. 7F). The bone volume/total volume (BV/TV) (Fig. 7G) and bone density (Fig. S22) indicate that the GCMS can eliminate the harmful effects of the infected microenvironment, resulting in a greater quantity of new bone formation. Moreover, heteromorphic devices featuring a metasurface galvanic cell were fabricated, exhibiting impressive antibacterial properties. The galvanic cell metasurface of PEEK-based (Fig. 7H) screws and (Fig. 7I) intervertebral cages has attractive antibacterial properties. PIII&PHS will be used for structure-function modification in electronic packages, flexible fibers, and 3D-printed polymers.

2.5. Osteogenic evaluation in vitro and in vivo

Cells on PEEK-ZrTi spread from spherical to filamentous pseudopods, adhering closely to the surface and eventually flattening into plate-like pseudopods (Fig. 8A). Cell spreading areas of PEEK-ZrTi gradually increase with culture time, and are higher than other samples (Fig. S23). Cytoskeletal staining further demonstrated that PEEK-ZrTi induced initial cell adhesion and spreading (Fig. S24). In addition, PEEK-ZrTi induces collagen secretion from stem cells and promotes extracellular matrix mineralization (Fig. 8B, Fig. S25). Alkaline phosphatase expression (ALP) is a marker of osteogenic differentiation. At 7 days, PEEK-ZrTi has the highest expression of ALP. At 14 days, PEEK-Zr explained the best ALP due to the osteogenic effect of the Zr element. However, PEEK-ZrTi was still significantly higher than PEEK and PEEK-Ti (Fig. S26). In contrast, cells retain the hemispherical morphology on the PEEK surface over time. The cell proliferation on the Zr/Ti bimetallic film is significantly higher than that of the monometallic metal films on Zr or Ti. However, monometallic films also have some pro-proliferation effects (Fig. 8C). At 1 day, the proliferation ratios of PEEK-Zr, PEEK-Ti, and PEEK-ZrTi were 55.42 %, 58.48 %, and 97.06 %, respectively (Fig. S27). In the gene analysis, the expression of ALP, BMP-2, and COL-1 genes in the PEEK-ZrTi group is significantly up-regulated (Fig. 8D). The osteogenic mechanism of GCMS involves rapid cell adhesion and proliferation on the surface due to the electroactive microenvironment (Fig. 8E) so the osteogenesis-related genes ALP, BMP-2, COL-1, and OCN expression are stimulated. PEEK-Zr has the highest expression of osteogenic genes, this is due to the Zr element itself having excellent osteogenic properties.

The immune response is the first physiological response initiated after foreign body implantation, and the immunoinflammatory properties contribute to creating a beneficial microenvironment. Compared to PEEK, the expression of the IL-10 gene, which is related to inflammation, significantly differed in the Zr/Ti bimetallic galvanic cell. However, there was no significant change in the expression of the IL-4 gene in PEEK-ZrTi. It suggests that galvanic cell metasurface can regulate

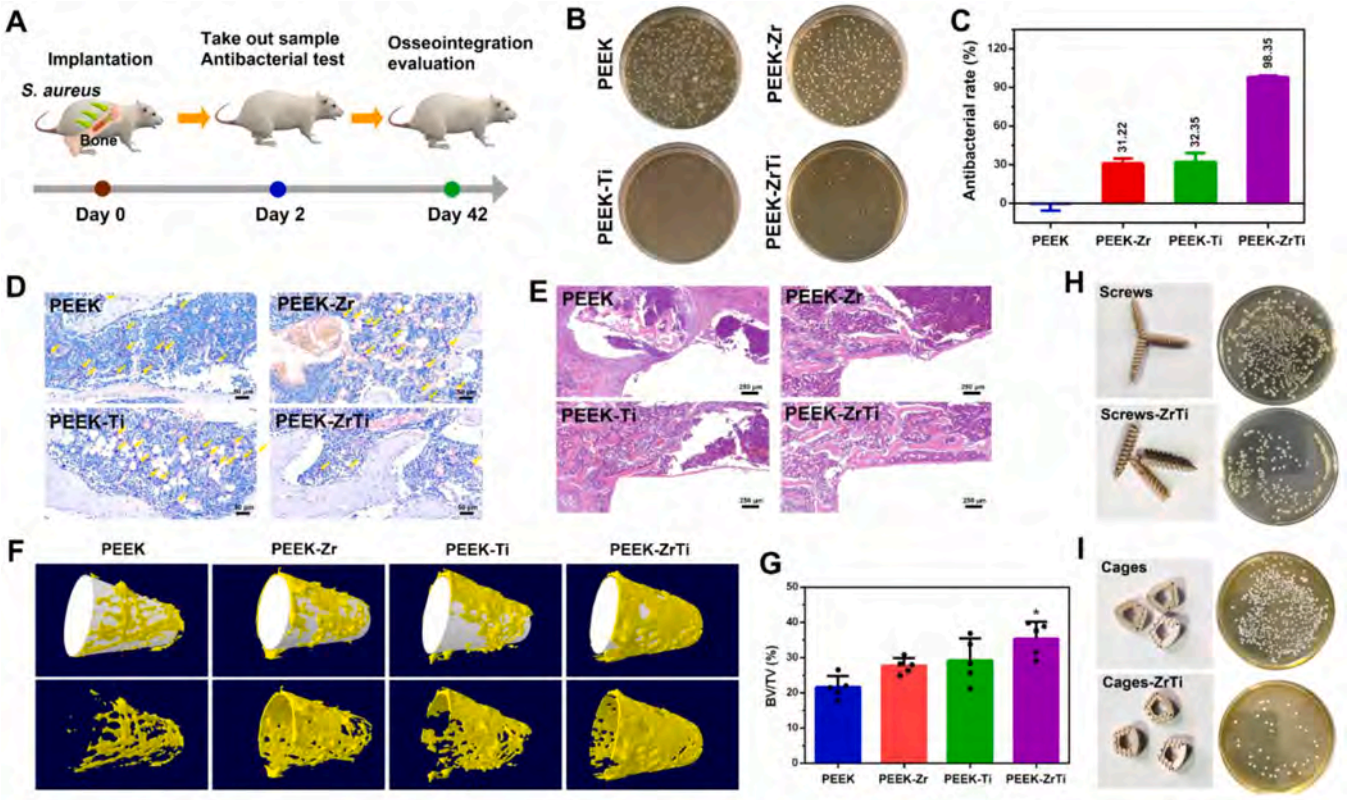

Fig. 7. Antibacterial properties of the galvanic cells metasurface *in vivo*. (A) Schematic diagram of the antibacterial model *in vivo*. The osteomyelitis model was used to evaluate osteointegration in the microenvironment of infection. (B) Photographs of colonies of *S. aureus* and (C) Corresponding antibacterial rate. (D) Giemsa staining and (E) H&E staining images of the bone tissues of the tibia around implants. The yellow arrows represent the bacteria. (F) 3D reconstruction images of the implants and newly formed bone around the implants. (G) Quantitative analysis of BV/TV based on micro-CT scanning. Photographs of colonies of *S. aureus* for (H) screws and (I) intervertebral cages with and without Zr/Ti GCMS.

inflammatory gene expressions (Fig. S28A). Further investigating the related gene about TLR4-MyD88-TRAF6-NF-κB1 signaling pathway of TNF-α secretion by macrophages on PEEK-ZrTi. The expression of MyD88, TRAF6, and NF-κB1 genes on the surface of PEEK-ZrTi significantly decreased, while there was no difference observed in TLR4 expression. This result demonstrates that the electroactive microenvironment had anti-inflammatory effects (Fig. S28A). Immune system secretions act as essential signaling molecules in osteogenesis. Therefore, the results of calcium deposition were evaluated using co-culture of macrophages and BMSCs. "Calcium nodules" formed on the PEEK-ZrTi bimetallic galvanic cell metasurface (Fig. S28B) and were markedly enhanced by modulating macrophage secretions (Fig. S28C). In conclusion, the electroactive microenvironment of the bimetallic galvanic cell was involved in regulating immune behavior.

The rat cranial defect model is used to evaluate the *in vivo* osseointegration of PEEK-ZrTi (Fig. 8F). The micro-CT of the skull 8 weeks shows that the cranial defect site was sealed in the PEEK-ZrTi group compared with PEEK (Fig. 8G). The percentages of bone volume were 20.82 % and 16.35 % for PEEK-ZrTi and PEEK implants, respectively. The bone trabecular densities of PEEK-ZrTi improved by 44.19 % than PEEK implants, respectively. This result significantly enhanced bone ingrowth on the surface of indicated PEEK-ZrTi galvanic cells. Similarly, the neoplastic bone contact area of PEEK-ZrTi also improved markedly (Fig. 8H). Sequential fluorescent labeling results illustrate that the PEEK-ZrTi group had a significant osteoinductive effect (Fig. S29). The osseointegration performance of PEEK-ZrTi GCMS is further evaluated in the tibial plateau of New Zealand white rabbits (Fig. 8I). The rabbit tibia is a weight-bearing bone, which is conducive to evaluating the potential application of PEEK-ZrTi film in weight-bearing bone defects. The mean torsional force of the PEEK-ZrTi was 150 N•mm, and about three times of that the PEEK group (50 N•mm) (Fig. 8J, Fig. S30A). Tripling the torque provides a significant advantage over the reported data [47,48]. This expounds that PEEK-ZrTi had a stronger one with the new bone interface. The micro-CT of the PEEK-ZrTi implant pointed out more new bone ingrowth than the PEEK implant (Fig. 8K). Quantitative analyses of both BV/TV were 12.28 % and 8.41 %, respectively (Fig. 8L). BS/TV also demonstrates the significant enhancement of osseointegration in the PEEK-ZrTi group (Fig. S30B). Van Gieson (VG) staining of rabbit femur shows that PEEK-ZrTi was tightly integrated with the surrounding bone tissues without fibrous tissue encapsulation (Fig. 8M). Based on the bone defect model and *in vitro* evaluation, the osteointegration capability of PEEK-ZrTi benefits from the electroactive surface and Zr element, inducing cell proliferation, osteogenic differentiation, and calcium deposition. Currently, many surface modification techniques for implants are not suitable for clinical polyhedron devices, making mass production challenging. It is expected that the GCMS implant can be commercialized for the mass production of heterogeneous devices, including intervertebral cage implants (Fig. 8N).

3. Conclusions

In summary, a bimetallic galvanic cell metasurface is fabricated by PIII&PHS on bio-polymers. Clinical-grade biosafe metals, Zr, Ti, and Ta exhibit pervasive surface electromobility. The galvanic cells are interconnected in parallel with the metasurface to achieve the "electron beam flow" effect. Bacteria adhere to the galvanic cell metasurface, where electrocatalysis produces up-regulation microenvironment ROS and disrupts the bacterial redox balance. The electron transfer between the bacterial membrane and the galvanic cells blocks proton transmembrane transport and ATP synthesis. Simultaneously, the

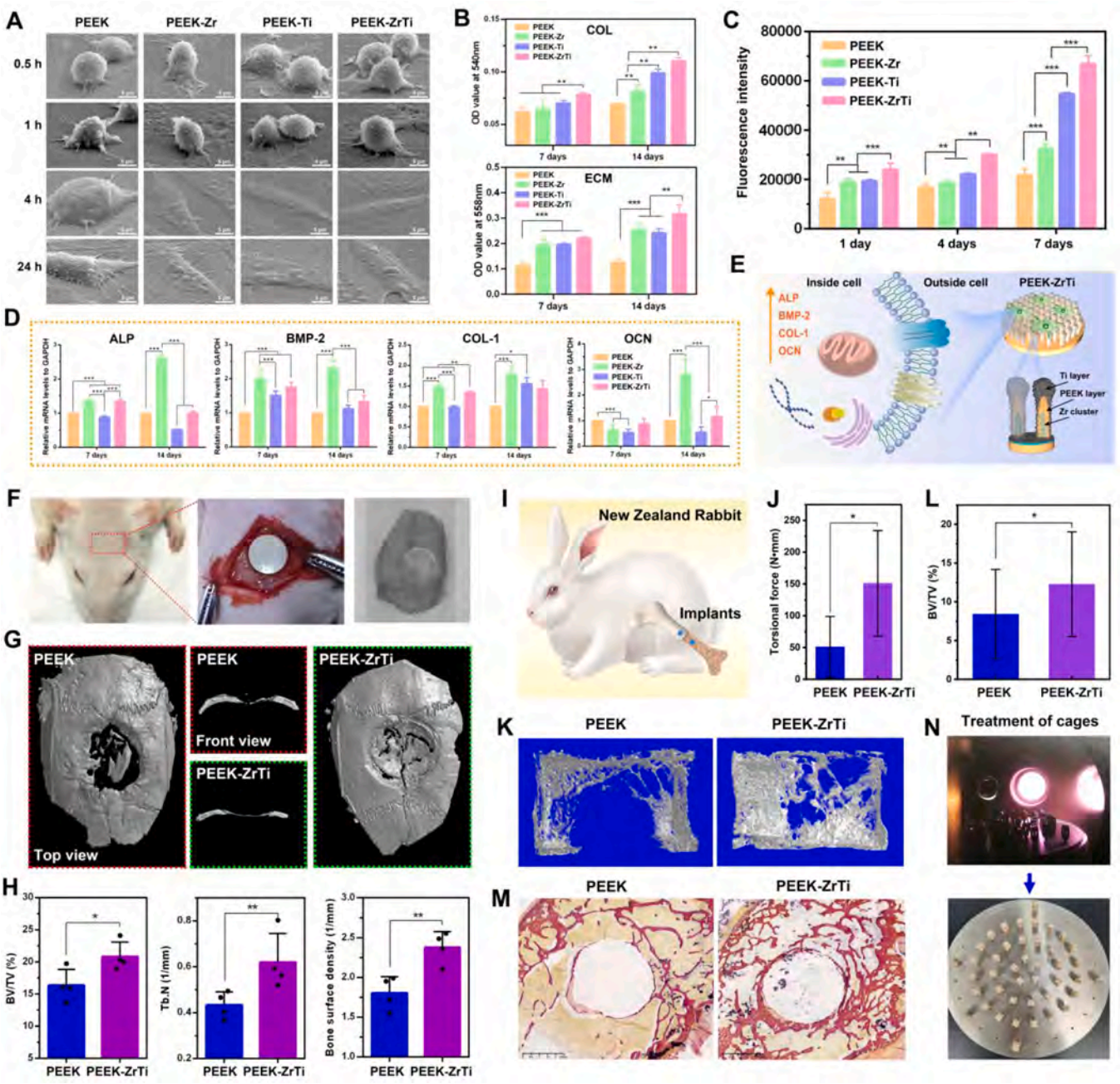

Fig. 8. The osteogenic properties of GCMS *in vitro* and *in vivo*. (A) BMSCs SEM morphology of various samples for 0.5, 1, 4, and 24 h. (B) Quantitative result of collagen (COL) and extracellular matrix mineralization (ECM). (C) Cell cultured on various samples proliferation, according to the alamarBlue assay. (D) Osteogenesis-related gene expression levels of BMSCs on various samples. (E) Schematic diagram of the mechanism of osteogenesis. (F) 3D micro-CT image of cranial defects generated in a rat model. (G) 3D Micro-CT images showing the radiological analysis of bone samples. (H) Quantitative analysis results of bone versus tissue volume (BV/TV), number of bone trabeculae, and bone surface density in a rat model. (I) Schematic diagram of the osseointegration for New Zealand rabbit. (J) The torsional force of the implants. (K) 3D micro-CT image of femoral defects generated in a rabbit model. (L) Quantitative analysis of BV/TV based on micro-CT scanning. (M) VG staining images of the bone tissues of the tibia samples 12 weeks after implantation. (N) Batch preparation of GCMS modification products based on PIII&PHS on commercial intervertebral cages. * : Compare with the PEEK group. Data represent means ± SD. Statistical significance was calculated by one-way ANOVA analysis. *$p < 0.05$; * *$p < 0.01$; * **$p < 0.001$.

electroactive microenvironment boosts the functionality of stem cells, indicating that the Zr/Ti galvanic cell metasurface holds potential as a bone substitute in rat and rabbit models. The galvanic cell metasurface implant is verified for the mass production of clinical devices. This study combines metamaterials innovation with the breakthrough of the electrochemical potential limits of bimetallic for the construction of highly biosafe metals.

4. Materials and methods

4.1. Preparation of galvanic cell metasurface

Medical PEEK materials were purchased from Jiangsu Junhua Company and processed into discs with Φ 12.5 mm × 1 mm and cylinders with Φ 2 mm × 8 mm. PEEK was polished and cleaned three times with acetone, alcohol, and ultrapure water, respectively.

The samples were placed in the PIII&PHS vacuum chamber. Zr PIII

was conducted using pulsed zirconium cathodic arc sources. Details of the treatment process are described in Table 1. The PHS technique is a joint surface nanosizing system that we developed based on PIII and the bipolar bias deposition technique proposed by Olbrich et al. [49] in 1991. Briefly, we enlarged the sample stage and added a bias power supply to serve as the sample stage for PIII and the target for PHS, respectively. After the completion of PIII, the sample stage changed its role and acted as the target for PHS (which can be changed arbitrarily according to the need for nanosizing). At this time, the bias voltage applied to the target (sample stage) led to the deposition of metal ions from the target by Ar ion sputtering onto the sample surface.

The combined system of PHS and PIII realizes the whole process of vacuum surface treatment, in addition to cleverly transforming the problem of contamination of the target material in the plasma coating into a highly efficient coating technology. This is a technical contribution to "turning waste into treasure". PHS was performed using Ar ion sputtering. Details of the treatment process are described in Table 2. Zr ion implanted PEEK, Ti deposited PEEK, and parallel Zr implanted and Ti deposited PEEK are labeled PEEK-Zr, PEEK-Ti, and PEEK-ZrTi, respectively. Arc sources of PIII and the target of PHS can be changed by the metals (M). The corresponding samples were named Substrate-M1M2. In particular, we popularized the PIII&PHS system for the surface nanosizing of PEKK, PASF, PAI, PEI, PTFE, and PPS substrates. The corresponding specimens were PEKK-ZrTi, PASF-ZrTi, PAI-ZrTi, PEI-ZrTi, PTFE-ZrTi and PPS-ZrTi.

To verify the surface properties of single metals in the presence of a metasurface, we took full advantage of the controllability of the PIII&PHS. Metal-PIII was replaced with Ar-PIII to achieve the metasurface with single metals. The monometallic metasurface samples were marked Meta-M (Meta-Zr, Meta-Ti, and Meta-Ta).

4.2. Materials characterization

Scanning electron microscopy (SEM) was performed on the SU8220 (HITACHI, Japan). Transmission electron microscopy (TEM) and elemental mapping were carried out by JEM-F200 (JEOL, Japan). The chemical composition and phases were examined by X-ray photoelectron spectroscopy (XPS, PHI-5000C ESCA System PerkinElmer, USA) and PANalytical X-ray diffractometer (XRD, D2 PHASER, Bruker, Germany). Inductively coupled plasma mass spectrometry determined the amounts of released ions (X Series 2, Thermofisher, USA). The surface wettability was measured by the contact angle (Automatic Contact Angle Meter Model SL200B, Solon, China). Electron paramagnetic resonance spectrometer (EPR, Bruker, A300X-band, USA) was used to identify the species of ROS. The Zeta potentials were measured by a surpass electrokinetic analyzer (SurPASS, Anton Paar, Austria). A multifunctional surface property tester (MFT-4000, China) was employed to analyze the friction and wear characteristics. The surface elastic modulus of the samples was tested using a Nanoindenter (Nano Indenter G200, Agilent, USA). The surface morphology and roughness of the films were characterized by AFM (Multimode 8, Bruker, Germany).

4.3. Electrical properties of galvanic cell metasurface

The four-probe method was investigated to test the surface current of the films. Briefly, a −4–4 V voltage was transferred to the film surface to detect the change in surface current. The distance between the electrodes was kept at 10 μm. The c-AFM (NTEGRA, NT-MDT, Russia) test system was used to examine the electrical properties of film microregions. A square area of 2 μm × 2 μm was selected, and the area current was analyzed after applying a voltage of 3 V. As the reaction substrate, TMB can be oxidized to blue ox-TMB by redox reaction, which will be utilized to evaluate the bimetallic galvanic cell characteristics. Briefly, samples, TMB (100 μL, 20 mM) and H2O2 (100 μL, 1 mM) were added into pH = 4 buffers successively and kept for 30 min at 37 °C. The absorbance peak of ox-TMB (550–750 nm) was recorded.

Table 1
Main conditions for Zr PIII.

Parameters	Description
Cathode source	99.99 % pure Zr
Voltage pulse duration (μs)	500
Pulsing frequency (Hz)	5
Voltage (kV)	−30
Time (min)	60
Pressure (Pa)	5×10^{-3}

Table 2
Main conditions for Ti PHS.

Parameters	Description
Sputtering target	99.99 % pure Ti
RF power (W)	300
Bias voltage(V)	1000
Duty cycle (%)	30
Time (min)	60
Pressure (Pa)	8×10^{-1}

4.4. Antibacterial evaluation in vitro

Gram-negative bacteria *E. coli* (ATCC 25922) and Gram-positive strain of *S. aureus* (ATCC 25923) were chosen to assess the antibacterial ability of the samples. Bacteria with a concentration of 1.0×10^6 CFU mL^{-1} were cultured at 37 °C for 24 h. Subsequently, the concentration of the bacteria solutions was diluted 100 times, and then 100 μL was taken to re-cultivate on agar plates at 37 °C. The formula for calculating the antibacterial efficiency is Antibacterial efficiency (%) = $(N_{Ctrl} - N_{Experiment})/N_{Ctrl} \times 100$ %.

The changes in bacterial morphology of various samples were observed via the SEM (S-3400N, HITACHI, Japan). The experimental steps refer to the previous study [16]. The ROS levels of bacteria were determined by the ROS Assay Kit (Beyotime, China) [50]. The part of bacterial extractions was surveyed using the PierceTM BCA Protein Assay Kit (Thermo Fisher Scientific, USA) to evaluate the extracellular concentration. The Enhanced ATP Assay Kit (Beyotime, China) was used to evaluate the level of ATP expression in bacterial cells.

4.5. Transcriptome analysis

After 1 day of incubation, *S. aureus* on PEEK and PEEK-ZrTi were collected and applied for RNA Sequencing by Majorbio (Shanghai, China). Total RNA was extracted from the bacteria using CTAB method and genomic DNA was removed. Only high-quality RNA sample was used to construct the sequencing library. Ribosomal RNA (rRNA) depletion instead of poly(A) purification is performed by RiboCop rRNA Depletion Kit for Mixed Bacterial Samples (Lexogen, USA) and then all mRNAs were broken into short (200nt) fragments by adding fragmentation buffer. Then, the RNA sequencing library was constructed and sequenced via an Illumina NovaSeq™ XPlus platform. Raw reads were filtered to obtain high-quality clean reads by removing reads with adapter, unknown, and low-quality sequences. Differently expressed genes (DEGs) usually interact with each other in vivo to play roles in certain biological functions. The significant DEGs were assigned into different functional groups following Gene Ontology GO and KEGG analysis.

4.6. Implant-associated osteomyelitis model in vivo

All animal procedures followed the Animal Management Rules of the Ministry of Health of the People's Republic of China and Guidelines for the Care and Use of Laboratory Animals of China. An osteomyelitis

model is used to evaluate the *in vivo* antibacterial activity of PEEK-ZrTi galvanic cell metasurface. The hair of the femur area of rats was removed and sterilized by iodophor wiping. A hole of Φ 2 mm was drilled along the bone marrow cavity using an electric drill, and 1×10^5 CFU mL^{-1} *S. aureus* was injected in 10 μL. Then, a sample of Φ 2 mm × 8 mm was implanted, subsequently sutured the wound and continued to be reared. Sprague Dawley (SD) rats (300–320 g) were randomly divided into four groups of PEEK, PEEK-Zr, PEEK-Ti, and PEEK-ZrTi. After 2 days of rearing, the samples were taken out for the agar plate antibacterial performance evaluation.

Six weeks after surgery, the osseointegration evaluation was conducted. The femurs with implants were scanned by micro-computed tomography (Micro Computed Tomography, SKYSCAN1076, Belgium). On the other hand, implant-contained femurs were decalcified. Then, the samples were embedded in paraffin wax and sliced into sections for immunohistochemical staining, and safranine-fast green staining was used to observe the tissue integration and new bone formation.

4.7. In vitro osteogenic evaluation

The osteogenic performances of the PEEK-ZrTi galvanic cell film toward MC3T3-E1 osteoblasts and rat Bone Marrow Stromal Cells (BMSCs) were seeded in samples. They were cultured in high-glucose cultured in α-minimum Eagle's medium (α-MEM) with 10 % fetal bovine serum (Gibco, USA) and 1 % penicillin-streptomycin (Gibco, USA). All cells were maintained at 37 °C in a humidified atmosphere with 5 % CO_2.

The cytocompatibility of the PEEK-ZrTi galvanic cell metasurface toward MC3T3-E1 osteoblasts was studied by the alamarBlue assay. The cell inoculation concentration was 2×10^4 cells mL^{-1}, and 10 % alamarBlue fresh medium was added after 1, 4, and 7 days of incubation, respectively. After incubation for 2 h, 100 μL of supernatant was aspirated to determine the emission wavelength (560 nm) and the excitation wavelength (590 nm).

MC3T3-E1 (2.0×10^4 cells mL^{-1}) were cultured on the samples to evaluate adhesion with 0.5, 1, 4, and 24 h, respectively. The cells on the samples were fixed with 2.5 % glutaraldehyde for 24 h and dehydrated sequentially in gradient ethanol (30 %, 50 %, 70 %, 90 %, 95 %, and 100 %). SEM was employed to observe cell morphology and ten cells were randomly counted to calculate the cell spreading area. Alternatively, samples were stained with DAPI and FITC-Phalloidin after incubation for 12 h. The Fluorescence microscope (Olympus, Japan) was used to investigate cytoskeletal differentiations.

The BMSCs were seeded on PEEK, PEEK-Zr, PEEK-Ti, and PEEK-ZrTi at a density of 1×10^4 cells $well^{-1}$ (cultured for 7 days) and 0.5×10^4 cells $well^{-1}$ (cultured for 14 days). The expression of ALP was evaluated using a BCIP/NBT ALP color development kit (Beyotime, China). The BSA protein concentration of each group was determined using a BCA kit (Beyotime, China). The relative activity of ALP was analyzed by normalizing the ALP concentration with the BSA protein concentration.

The BMSCs were seeded on PEEK, PEEK-Zr, PEEK-Ti, and PEEK-ZrTi at a density of 1×10^4 cells $well^{-1}$ (cultured for 7 days) and 0.5×10^4 cells $well^{-1}$ (cultured for 14 days). The samples were fixed with 4 % paraformaldehyde and stained with Sirius Red for 18 h. Staining qualitative results were obtained using fluorescence microscope photography. To analyze the quantitative results, the dye was eluted (V (0.2 mol L^{-1} NaOH): V (methanol) = 1: 1), and the OD value of the eluate at 540 nm was tested.

The BMSCs were cultured as mentioned above. At 7 and 14 days, The cells were stained with alizarin red stain for 10 minutes and rinsed repeatedly with ultrapure water until the solution was colorless. A microscope system (Olympus, Japan) was used to observe the stained Alizarin Red. Afterward, the solution was measured by detecting the absorbance at a wavelength of 558 nm using a microplate reader (Bio-Tek, USA).

On the gene expression level, Osteogenic genes such as ALP, BMP-2, COL-1, and OCN were evaluated by quantitative real-time PCR (qPCR). Briefly, the BMSCs seeded on various samples were cultured for 7 and 14 days. 1 mL Trizol reagent (Invitrogen, Thermo Fisher Scientific Inc., USA) was used to extract RNA from the cells. Transcriptor First Strand cDNA Synthesis Kit (Roche, Switzerland) was used to synthesize cDNA from 1 μg total RNA. FastStart Universal SYBR Green I Master Mix (Roche, Switzerland) was used in qPCR on the LightCycler480® system (Roche, Switzerland). The primers (BioTNT) sequences for qPCR are listed in Table S2.

The macrophage (RAW.264.7) was used to evaluate immune behavior. RT-qPCR was tested and cultured for 4 days. The cells were then collected using TRIzol™. RT-qPCR used the LightCycler 480 system with glyceraldehyde-3-phosphate dehydrogenase (GAPDH) as the reference gene, and the primers were listed in Table S3. RAW.264.7 was cultured and co-cultured with BMSC. The samples were fixed with 4 % paraformaldehyde and stained with Sirius Red for 18 h. Staining qualitative results were obtained using fluorescence microscope photography. The OD value of the eluate at 540 nm was tested for quantitative results.

4.8. In vivo bone regeneration

The Animal Experiment Theory Committee of Shanghai Changzheng Hospital approved the rat cranial defect implantation model in this work. The SD rats (200–250 g) were randomly divided into four groups, eight in each group. A curved incision was made in the cranial area between the two ears to expose the skull. After that, a defect area with a diameter of 7 mm and a depth of about 0.5 mm was ground out in the middle of the skull using a diamond ball drill, and then PEEK, PEEK-Zr, PEEK-Ti, and PEEK-ZrTi samples were placed into the defect location. Experiments were performed to characterize new bone and mineralization using polychrome sequential fluorescent labeling method (polychrome sequential fluorescent labeling method). Eight weeks later, rat skulls were collected and fixed in a 4 % paraformaldehyde buffer solution for micro-CT reconstruction and quantitative analysis of bone regeneration.

The experiment used male New Zealand rabbits, aged 6–7 months, weighing 3.5–4.5 kg. A 3 % pentobarbital sodium was taken at a dose of 1 mL/kg, and anesthesia was slowly pushed through the marginal vein of the ear. The knee joint of the experimental rabbit was located, and a longitudinal incision of about 2 cm was made on the lateral skin to expose the femoral condyle. A hole was created using a 5 mm bone drill, into which the implant material was inserted, followed by suturing of the skin. Eight weeks after the operation, the experimental rabbits were euthanized, and the bilateral femurs were taken as subsequent detection samples. Micro-CT was used to detect and evaluate the new bone condition of the samples. A complete specimen of the surgical site was taken, muscle and skin tissues were removed, and the complete skeleton was retained. Then, the samples were embedded in paraffin wax and sliced into sections for immunohistochemical staining to observe tissue integration and new bone formation. The SANS mechanical measuring instrument was used to test the torque change when rotating the material, draw the twisting curve, and record the maximum torque for statistics.

4.9. Statistical analysis

A GraphPad Prism 6.0 statistical software measured the mean ± standard deviation (SD). Data was compared via one-way ANOVA and post hoc Tukey's test. *$p < 0.05$, * *$p < 0.01$, and * **$P < 0.001$ were considered statistically significant.

CRediT authorship contribution statement

Shiwei Guan: Writing-review & editing, Writing-original draft, Methodology, Validation, Investigation, Formal analysis, Data curation.

Zhiyu Hou: Writing-review & editing, Methodology, Data curation, Formal analysis. **Xianming Zhang:** Writing-review & editing, Methodology. **Yuanming Cao:** Data curation, Methodology. **Shi Qian:** Investigation, Data curation. **Xingdan Liu:** Writing-review & editing, Software. **Fang Wang:** Data curation, Methodology. **Hongqin Zhu:** Methodology. **Dandan Li:** Methodology, Formal analysis. **Paul K Chu:** Resources, Project administration, Methodology, Funding acquisition. **Ji Tan:** Conceptualization, Investigation, Methodology, Project administration, Writing-review & editing. **Xuanyong Liu:** Resources, Project administration, Funding acquisition, Conceptualization, Writing-review & editing.

Declaration of Competing Interest

The authors declare that they have no known competing financial interests or personal relationships that could have appeared to influence the work reported in this paper.

Acknowledgements

This work has been supported by the “Pioneer” and “Leading Goose” R&D Program of Zhejiang (2024C03080), National Natural Science Foundation of China (U21A20100), Shenzhen Science and Technology Funding (JCYJ20210324120009026), and City University of Hong Kong Donation Research Grants (DON-RMG No. 9229021 and 9220061).

Appendix A. Supporting information

Supplementary data associated with this article can be found in the online version at doi:10.1016/j.mser.2025.100929.

Data availability

Data will be made available on request.

References

[1] J. Min, K.Y. Choi, E.C. Dreaden, R.F. Padera, R.D. Braatz, M. Spector, P. T. Hammond, ACS Nano 10 (2016) 4441–4450.
[2] L. Tan, J. Fu, F. Feng, X. Liu, Z. Cui, B. Li, Y. Han, Y. Zheng, K.W.K. Yeung, Z. Li, S. Zhu, Y. Liang, X. Feng, X. Wang, S. Wu, Sci. Adv. 6 (2020) eaba5723.
[3] C.R. Arciola, D. Campoccia, L. Montanaro, Nat. Rev. Microbiol. 16 (2018) 397–409.
[4] J. Liao, W. Chen, M. Yang, J. Zhou, Z. Wang, Y. Zhou, C. Ning, H. Yuan, Mater. Horiz. 5 (2018) 545–552.
[5] S. Panda, T.K. Rout, A.D. Prusty, P.M. Ajayan, S. Nayak, Adv. Mater. 30 (2018) 1702149.
[6] E.S. Sani, R.P. Lara, Z. Aldawood, S.H. Bassir, D. Nguyen, A. Kantarci, G. Intini, N. Annabi, Matter 1 (2019) 926–944.
[7] S. Chernousova, M. Epple, Angew. Chem. Int. Ed. 52 (2012) 1636–1653.
[8] E.A. Masters, B.F. Ricciardi, K.Ld.M. Bentley, T.F. Moriarty, E.M. Schwarz, G. Muthukrishnan, Nat. Rev. Microbiol. 20 (2022) 385–400.
[9] B. Li, W. Wang, L. Zhao, Y. Wu, X. Li, D. Yan, Q. Gao, Y. Yan, J. Zhang, Y. Feng, J. Zheng, B. Shu, J. Wang, H. Wang, L. He, Y. Zhang, M. Pan, D. Wang, B.Z. Tang, Y. Liao, Nat. Nanotechnol. 19 (2024) 834–845.
[10] G. Wang, K. Tang, Z. Meng, P. Liu, S. Mo, B. Mehrjou, H. Wang, X. Liu, Z. Wu, P. K. Chu, Adv. Mater. 32 (2020) e2003616.
[11] D. Wang, J. Tan, H. Zhu, Y. Mei, X. Liu, Adv. Sci. (2021) e2004393.
[12] J. Fu, W. Zhu, X. Liu, C. Liang, Y. Zheng, Z. Li, Y. Liang, D. Zheng, S. Zhu, Z. Cui, S. Wu, Nat. Commun. 12 (2021) 6907.
[13] S.H. Light, L. Su, R. Rivera-Lugo, J.A. Cornejo, A. Louie, A.T. Iavarone, C.M. Ajo-Franklin, D.A. Portnoy, Nature 562 (2018) 140–144.
[14] L. Shi, H. Dong, G. Reguera, H. Beyenal, A. Lu, J. Liu, H.-Q. Yu, J.K. Fredrickson, Nat. Rev. Microbiol. 14 (2016) 651–662.
[15] G. Reguera, K.D. McCarthy, T. Mehta, J.S. Nicoll, M.T. Tuominen, D.R. Lovley, Nature 435 (2005) 1098–1101.
[16] H. Cao, K. Tang, X. Liu, Mater. Horiz. 5 (2018) 264–267.
[17] H. Strahl, L.W. Hamoen, Proc. Natl. Acad. Sci. 107 (2010) 12281–12286.
[18] I.Y. Suh, Z.Y. Huo, J.H. Jung, D. Kang, D.M. Lee, Y.J. Kim, B. Kim, J. Jeon, P. Zhao, J. Shin, S. Kim, S.W. Kim, Sci. Adv, 2024, p. eadl5067.
[19] K.Y. Kwon, S. Cheeseman, A. Frias-De-Diego, H. Hong, J. Yang, W. Jung, H. Yin, B. J. Murdoch, F. Scholle, N. Crook, E. Crisci, M.D. Dickey, V.K. Truong, T.I. Kim, Adv. Mater. 33 (2021) e2104298.
[20] T.T. Nguyen, P. Zhang, J. Bi, N.H. Nguyen, Y. Dang, Z. Xu, H. Wang, N. Ninan, R. Bright, T. Pham, C.K. Nguyen, Y. Sabri, M.T. Nguyen, J. Vongsvivut, Y. Zhao, K. Vasilev, V.K. Truong, Adv. Funct. Mater. 34 (2023).
[21] Y. Tang, K. Wang, B. Wu, K. Yao, S. Feng, X. Zhou, L. Xiang, Adv. Mater, 2023.
[22] G. Fichman, C. Andrews, N.L. Patel, J.P. Schneider, Adv. Mater. 33 (2021) e2103677.
[23] W. Liu, K. Zhang, Y. Sun, Z. Xiao, H. Hu, Z. Xiong, Y. Hu, Bioact. Mater. 44 (2025) 15–33.
[24] Y. Luo, J. Li, X. Liu, L. Tan, Z. Cui, X. Feng, X. Yang, Y. Liang, Z. Li, S. Zhu, Y. Zheng, K.W.K. Yeung, C. Yang, X. Wang, S. Wu, ACS Cent. Sci. 5 (2019) 1591–1601.
[25] J. Lu, H. Zhang, J. Hou, X. Li, X. Hu, Y. Hu, C.D. Easton, Q. Li, C. Sun, A. W. Thornton, M.R. Hill, X. Zhang, G. Jiang, J.Z. Liu, A.J. Hill, B.D. Freeman, L. Jiang, H. Wang, Nat. Mater. 19 (2020) 767–774.
[26] J. Bullock, M. Hettick, J. Geissbühler, A.J. Ong, T. Allen, C.M. Sutter-Fella, T. Chen, H. Ota, E.W. Schaler, S. De Wolf, C. Ballif, A. Cuevas, A. Javey, Nat. Energy 1 (2016) 15031.
[27] H. Wu, Y. Wang, H. Li, Y. Hu, Y. Liu, X. Jiang, H. Sun, F. Liu, A. Xiao, T. Chang, L. Lin, K. Yang, Z. Wang, Z. Dong, Y. Li, S. Dong, S. Wang, J. Chen, Y. Liu, D. Yin, H. Zhang, M. Liu, S. Kong, Z. Yang, X. Yu, Y. Wang, Y. Fan, L. Wang, C. Yu, L. Chang, Nat. Electron. 7 (2024) 299–312.
[28] J. Cha, K.W. Kim, C. Daraio, Nature 564 (2018) 229–233.
[29] H. Keuer, C. Ganz, W. Xu, A. Schubert, B. Frerich, T. Gerber, Osteoinductive coating on PEEK surfaces by using nanocrystalline biomaterial and *in vivo* test, 24th Symposium and Annual Meeting of International Society for Ceramics in Medicine (ISCM 2012), vol 529-530, Fukuoka, JAPAN, 2012, pp. 345-+ .
[30] S.M. Kurtz, J.N. Devine, Biomaterials 28 (2007) 4845–4869.
[31] H. Wang, X. Fu, J. Shi, L. Li, J. Sun, X. Zhang, Q. Han, Y. Deng, X. Gan, Adv. Sci. 8 (2021) e2101778.
[32] X. Xu, Y. Li, L. Wang, Y. Li, J. Pan, X. Fu, Z. Luo, Y. Sui, S. Zhang, L. Wang, Y. Ni, L. Zhang, S. Wei, Biomaterials 212 (2019) 98–114.
[33] Z. Yuan, L. Liang, Q. Dai, T. Li, Q. Song, H. Zhang, G. Hou, X. Li, Joule 6 (2022) 884–905.
[34] H. Wang, J. Tian, Y. Jiang, S. Liu, J. Zheng, N. Li, G. Wang, F. Dong, J. Chen, Y. Xie, Y. Huang, X. Cai, X. Wang, W. Xiong, H. Qi, L. Yin, Y. Wang, X. Sheng, Sci. Adv. 9 (2023) eabq7750.
[35] K. Birsoy, T. Wang, W.W. Chen, E. Freinkman, M. Abu-Remaileh, D.M. Sabatini, Cell 162 (2015) 540–551.
[36] B. Dashtbozorg, F. Shi, A. Tagliaferro, S. Abela, L. Falticeanu, H. Dong, Acta Mater. 262 (2024) 119457.
[37] J.R. Atkinson, J.N. Hay, M.J. Jenkins, Polymer 43 (2002) 731–735.
[38] Y. Shin, S. Hong, Y.C. Hur, C. Lim, K. Do, J.H. Kim, D.-H. Kim, S. Lee, Nat. Mater. (2024).
[39] T.E. Sheridan, T.K. Kwok, P.K. Chu, Appl. Phy. Lett. 72 (1998) 1826–1828.
[40] T.E. Sheridan, J. Appl. Physiol. 74 (1993) 4903–4906.
[41] H. Zhao, Y. Chen, Q. Peng, Q. Wang, G. Zhao, Appl. Catal. B Environ. 203 (2017) 127–137.
[42] J.P. MacArthur, J. Duris, Z. Zhang, A. Lutman, A. Zholents, X. Xu, Z. Huang, A. Marinelli, Phys. Rev. Lett. 123 (2019) 214801.
[43] S. Daqiqeh Rezaei, J. Ho, T. Wang, S. Ramakrishna, J.K.W. Yang, Nano Lett. 20 (2020) 4422–4429.
[44] J.A. Lemire, J.J. Harrison, R.J. Turner, Nat. Rev. Microbiol. 11 (2013) 371–384.
[45] D.R. Lovley, J.D. Coates, E.L. BluntHarris, E.J.P. Phillips, J.C. Woodward, Nature 382 (1996) 445–448.
[46] S.Y. Reece, D.G. Nocera, Annu. Rev. Biochem. 78 (2009) 673–699.
[47] S. Sharma, V. Gupta, D. Mudgal, Polymer International, 2024.
[48] S. Sharma, D. Mudgal, V. Gupta, Biopolymers 115 (2024) e23600.
[49] W. Olbrich, J. Fessmann, G. Kampschulte, J. Ebberink, Surf. Coat. Technol. 49 (1991) 258–262.
[50] L. Wu, J. Tan, S. Chen, X. Liu, Chem. Eng. J. 447 (2022) 137484.

Shiwei Guan received his PhD degree in materials science from the Shanghai Institute of Ceramics, Chinese Academy of Sciences in 2024. He currently works at The University of Hong Kong. His main research focuses on coating/film titanium and polymer implants, antimicrobial and osteogenic materials, and wound repair with hydrogel.

Ji Tan was born in 1994. He received his BE degree in materials science and engineering from Hainan University in 2015, and received PhD degree in materials science from Shanghai Institute of Ceramics, Chinese Academy of Sciences (SICCAS) in 2020. he has worked as a Postdoctoral Researcher at SICCAS in 2020–2023. He is now an associated professor at SICCAS. His current research interests focus on the biological effects of material surface and interface, and the surface modification of biomedical implants.

Xuanyong Liu received his BS and MS in materials science and engineering from Hunan University in 1996 and 1999 respectively and PhD in materials science and engineering from Shanghai Institute of Ceramics Chinese Academy of Sciences, in 2002. He is a professor and the director of the Biomaterials and Tissue Engineering Research Center in SICCAS. He was elected as Fellow, Biomaterials Science and Engineering (FBSE) by The International Union of Societies for Biomaterials Science and Engineering (IUSBSE) in 2020, and the Fellow of the Chinese Society for Biomaterials, FCSBM in 2023. His primary research interests include biomaterials surface and interface, antibacterial/antitumor materials, and bone/wound repair materials. Up to now, he has published over 400 peer-reviewed papers with h-index of 72 and total citation of over 20000 times.

Supplementary materials

Galvanic cell metasurface modulating electron transfer on polymer implants for sterilization and osteointegration

Shiwei Guan[1#], Zhiyu Hou[1#], Xianming Zhang[1], Yuanming Cao[2], Shi Qian[1], Xingdan Liu[1], Fang Wang[1], Hongqin Zhu[1], Dandan Li[1], Paul K Chu[4], Ji Tan[1*], and Xuanyong Liu[1,2,3*]

[1] State Key Laboratory of High Performance Ceramics and Superfine Microstructure, Shanghai Institute of Ceramics, Chinese Academy of Sciences, Shanghai 200050, China

[2] College of Biological Science and Medical Engineering, Donghua University, Shanghai 201620, China.

[3] School of Chemistry and Materials Science, Hangzhou Institute for Advanced Study, University of Chinese Academy of Sciences, 1 Sub-lane Xiangshan, Hangzhou 310024, China

[4] Department of Physics, Department of Materials Science & Engineering, and Department of Biomedical Engineering, City University of Hong Kong, Tat Chee Avenue, Kowloon, Hong Kong, China

[*]**Corresponding Auther:**

Prof. Xuanyong Liu, E-mail: xyliu@mail.sic.ac.cn

Dr. Ji Tan, E-mail: tanji@mail.sic.ac.cn

1. Calculation of PIII&PHS technical principle

The negative bias applied to the target is V_t, and the potential on the sample surface is V_s. In the plasma near the target, positive ions with a potential V_t bombard the target to produce sputtering.

In an RF-ionized Ar plasma, an electric field is created between the samples and the target to generate a plasma sheath. Ar ions then bombard the target and sputter ions and atoms. The ions with part atoms of the sheath are drawn to the sample surface under the bias potential. In PIII&PHS, the samples and target are located at the same cathode and subjected to ion sputtering and deposition.

Polymer samples are insulating materials and exhibit capacitive properties of charge accumulation, which consumes some of the bias potential. Therefore

$$V_s < V_t. \tag{S1}$$

At the start of the PHS, the sample surface has the highest surface permittivity ($\Delta\varepsilon_s$) with the most charge accumulation. As metal deposition increases, $\Delta\varepsilon_s$ gradually decreases, i.e., the surface capacitance dynamically changes. The surface charge accumulation U_s is shown below:

$$U_s = k \times \frac{\Delta\varepsilon_s}{d}\ , \tag{S2}$$

where k is a constant, $\Delta\varepsilon_s$ is the dynamic permittivity, and d is the medium distance. Therefore, the bias pressure effectively acting on the sample surface is as follows:

$$V_s = V_t - U_s. \tag{S3}$$

When the sample is negatively biased relative to the plasma potential, a plasma sheath of a certain thickness is formed. The ion current is determined by the plasma source.

$$S_{Child} = \frac{\sqrt{3}}{3}\lambda_{De}\left(\frac{2eV_s}{kT_e}\right)^{3/4}, \tag{S4}$$

where S_{Child} is the sheath thickness, T_e is the electron temperature, e is the electron charge,

k is the Boltzmann constant, and λ_{De} is the Debye length [1].

$$\lambda_{De} = \sqrt{\frac{\varepsilon_0 k T_e}{n_0 e^2}}\ , \tag{S5}$$

where ε_0 is the permittivity of free space, k is Boltzmann's constant, T_e is the electron temperature, e is the electron charge, and n_0 is the plasma density.

The plasma sheath is filled with electrons and ions. According to the Child-Langmuir law [2], the density of ion flow j_i in the sheath is Equation S6：

$$j_i = \frac{4}{9}\varepsilon_0\sqrt{\frac{2e}{m_i}}\frac{V_s^{3/2}}{S}, \tag{S6}$$

where S is the spacing of the fixed positive and negative electrodes, the sheath ion flow density j_i is proportional to $V_s^{3/2}$.

There are two processes in the plasma sheath, one in which the target is sputtered to deposited onto the sample surface, and the other in which the film deposited is re-sputtered out of the sample. Assuming that all sputtered material is deposited onto the samples, the deposition rate Q for PHS is Equation S7 [3]

$$Q = AC\gamma j_i, \tag{S7}$$

where γ is the target sputtering yield, j_i is the incident ion flow density, A is the polymer samples characteristic, and C represents the parameter for the target properties. A and C can be taken as a constant.

$$Q_s = AC\gamma(j_{iT} - j_{iS}), \tag{S8}$$

where Q_s is the deposition rate of the sample surface in the sheath, and j_{iS} and j_{iT} represent the densities of ion flow of the sample and target, respectively.

As shown in Fig. 3D (v), the polymer sample accumulates a large amount of charge. We can assume that $j_{iS} \approx 0$, because the surface is insulating ($\Delta\varepsilon_s$ maximum). Therefore, $Q_s = AC\gamma j_{iT}$. As the metal is deposited on the sample surface, $\Delta\varepsilon_s$ gradually decreases, $j_{iT} > j_{iS}$ leading to Q_s decrease. When $j_{iT} = j_{iS}$, $Q_s 00$, the metal deposition reaches dynamic

equilibrium with sputtering on the sample surface.

2. Metasurface growth mechanism

As shown in Fig. 3D (v), the gap of the metasurface nanopillar array can be approximated as a nanotube-like structure with diameter d. The deposition rate (Q_s) at the inner wall of the nanotube during PHS application is hindered by the potential drop inside the pore [1, 4]. If the nanotube-like radius $\mathrm{d}/2$ is less than the ion-matrix overlap length, the critical value of the spacing distance (D_d) can be acquired by [5]

$$D_d = (\frac{-2\varepsilon_0\varphi}{en_e})^{1/2}, \tag{S9}$$

where $\mathrm{n_e}$ is the plasma density, φ is the bias potential applied to the target, ε_0 is the permittivity of free space, and e is the electronic charge. The potential drop $\Delta\varphi$ can be exported to

$$\Delta\varphi = ((\mathrm{d}/2)/\mathrm{D_d})^2\varphi \ . \tag{S10}$$

The potential drop $\Delta\varphi$ in the pores implies that the plasma accumulates below the surface of the columnar protrusions left behind by the PIII process. Consequently, the columnar protrusions become sites for selective deposition (Fig. 3D (v)). Nanopillars grow dynamically to form a metasurface with nanopillar spacing $\mathrm{d}/2 < \mathrm{D_d}$.

3. Supplementary results

The supplementary results mainly include structure-composition analysis, osteointegration, antibacterial and gene expression results of the galvanic cell metasurfaces.

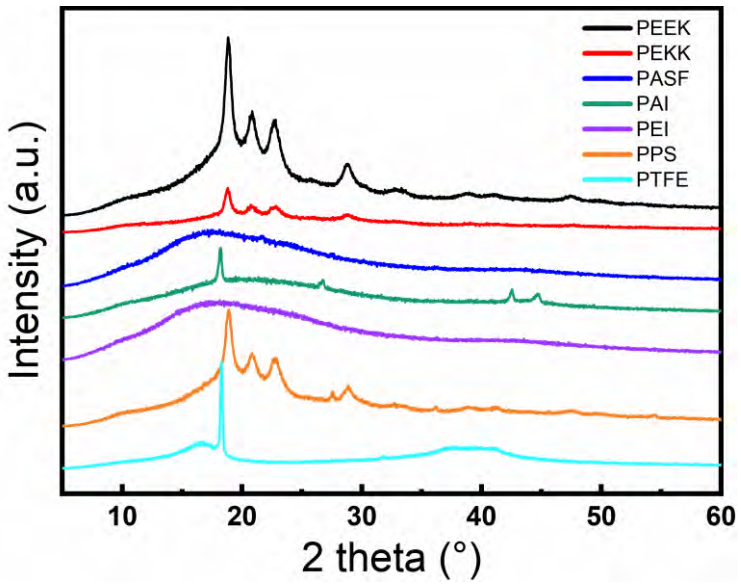

Fig. S1. XRD patterns of PEEK, PEKK, PASF, PAI, PEI, PPS, and PTFE.

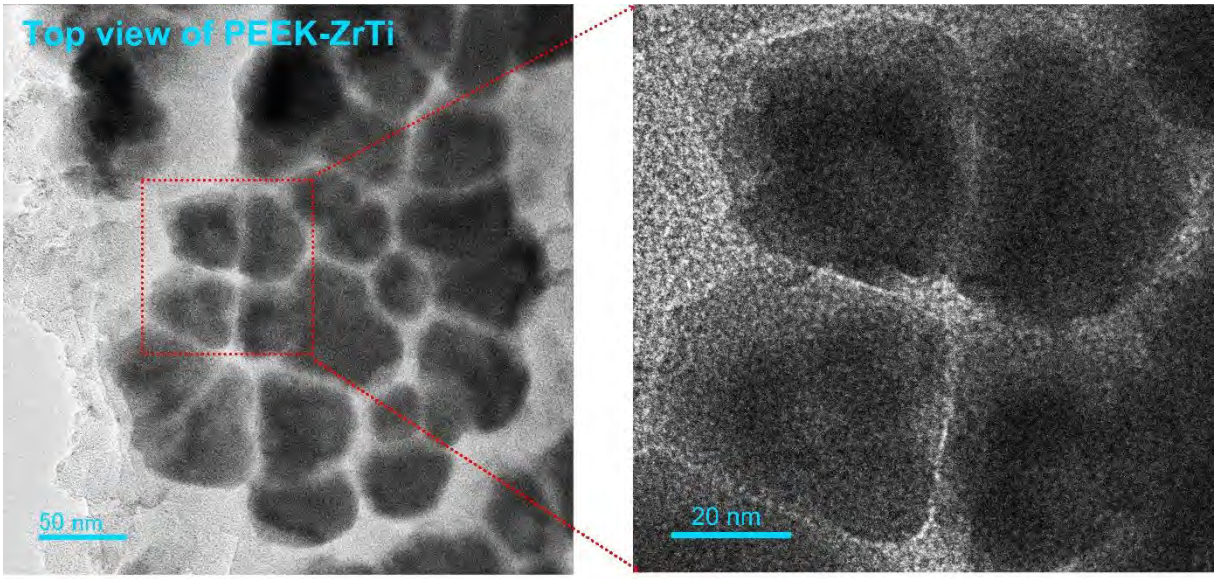

Fig. S2. HR-TEM images of top view for PEEK-ZrTi.

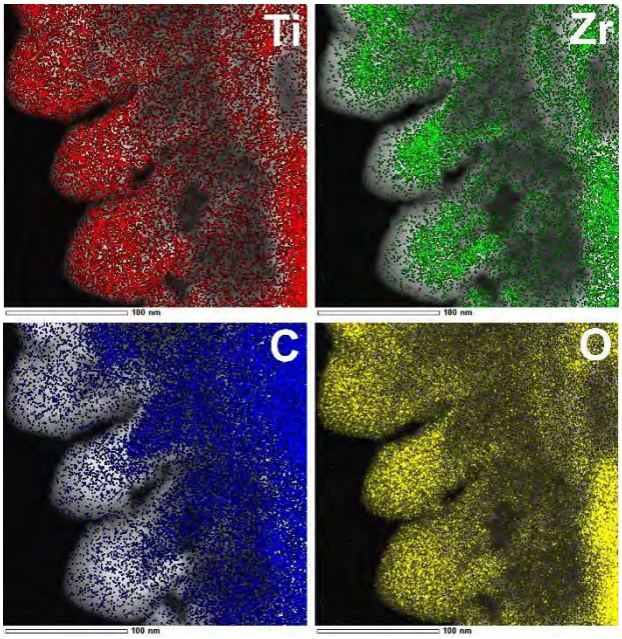

Fig. S3. The EDS mapping of the cross-section for PEEK-ZrTi with TEM.

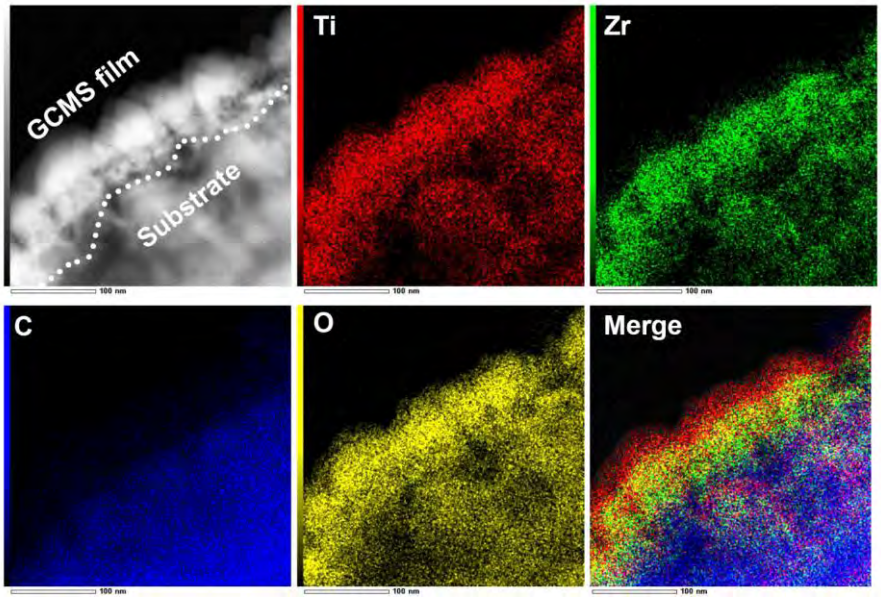

Fig. S4. The EDS mapping of the cross-section for PEEK-ZrTi at low magnification.

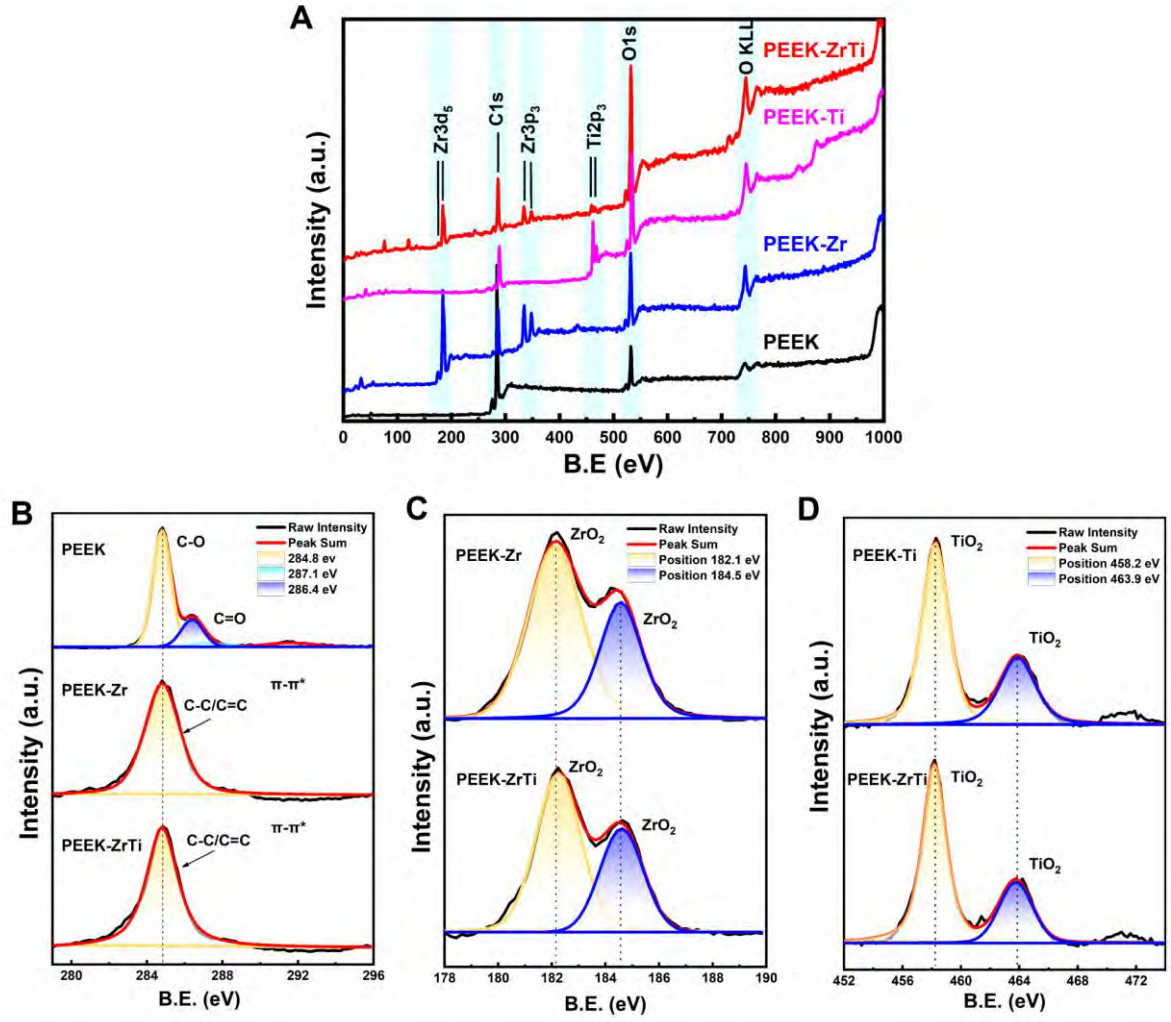

Fig. S5. (A) XPS full spectra. XPS high-resolution spectra of (B) C 1*s*, (C) Zr 3*d*, and (D) Ti 2*p* of the samples.

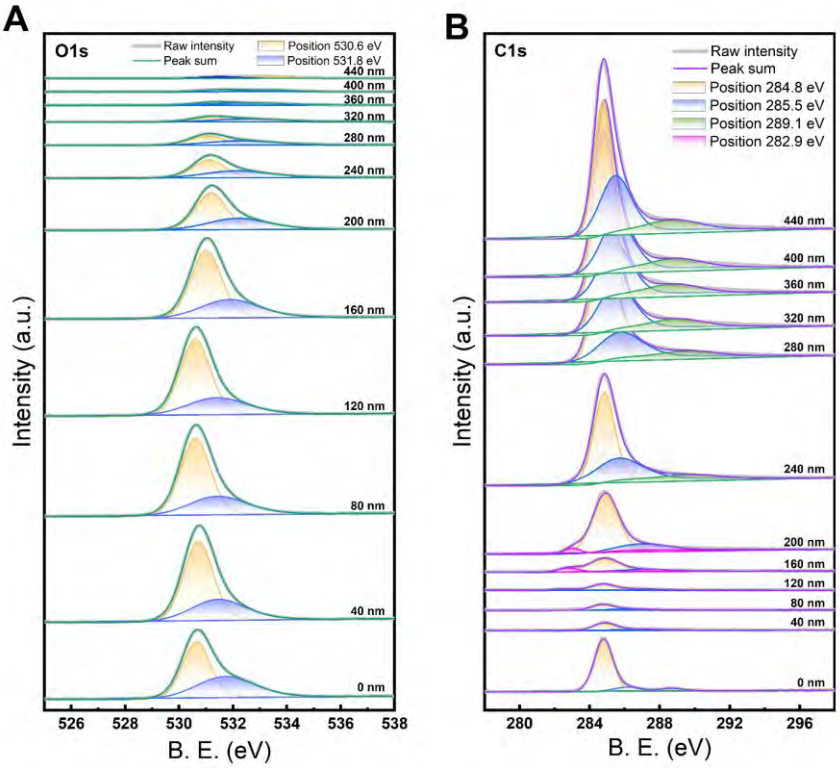

Fig. S6. (A) O 1*s* and (B) C 1*s* spectra of PEEK-ZrTi at various depths by XPS.

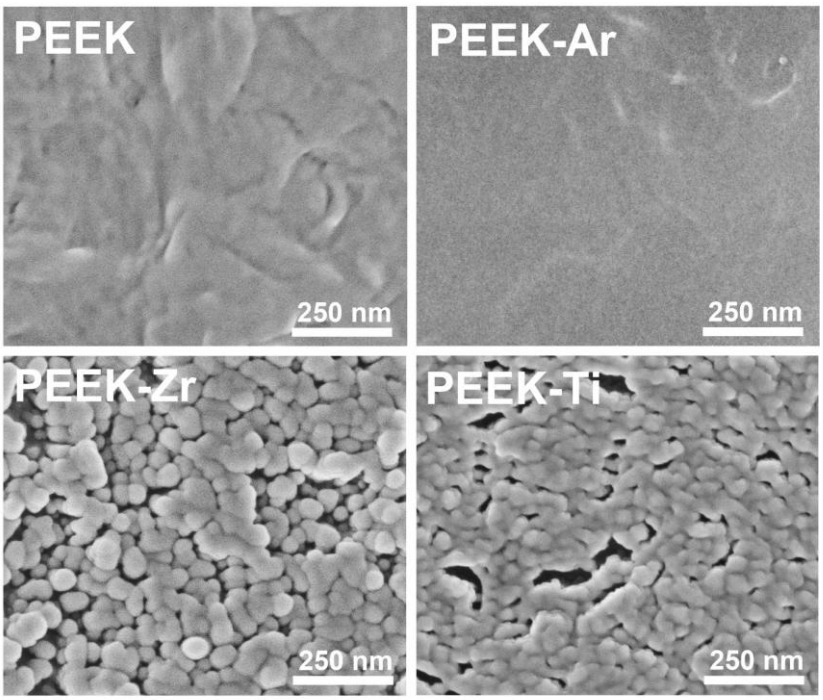

Fig. S7. SEM images of PEEK, PEKK-Ar, PEEK-Zr, and PEEK-Ti.

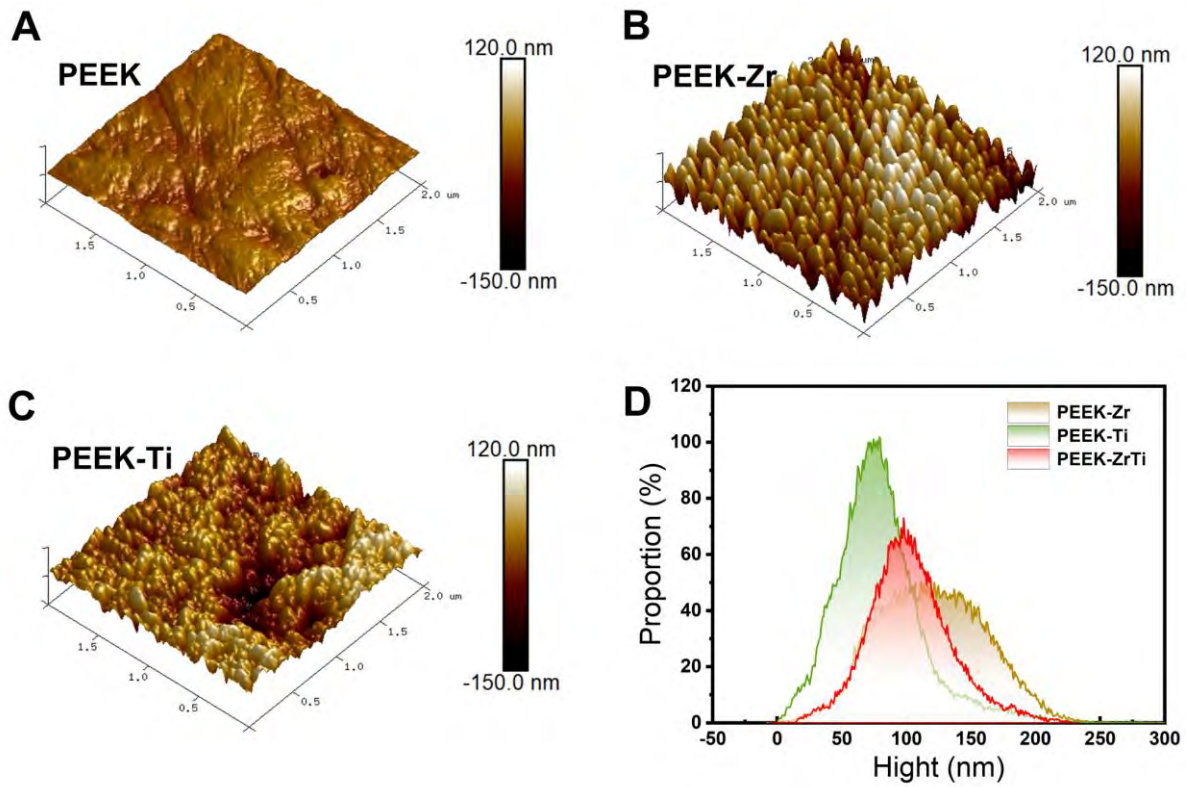

Fig. S8. AFM images of (A) PEEK, (B) PEEK-Zr, and (C) PEEK-Ti. (D) Distribution of nanopillar heights on the sample surface. It was obtained from the statistical analysis of the AFM results.

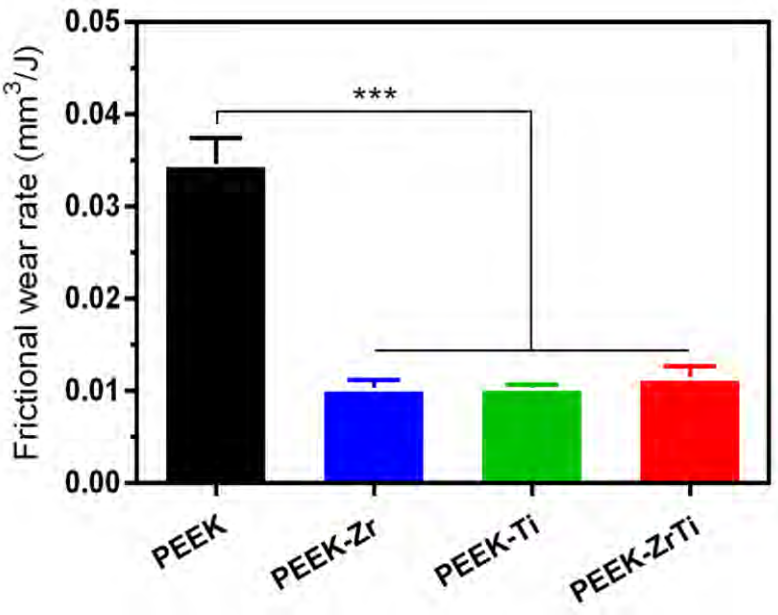

Fig. S9. The frictional wear rate of the various samples.

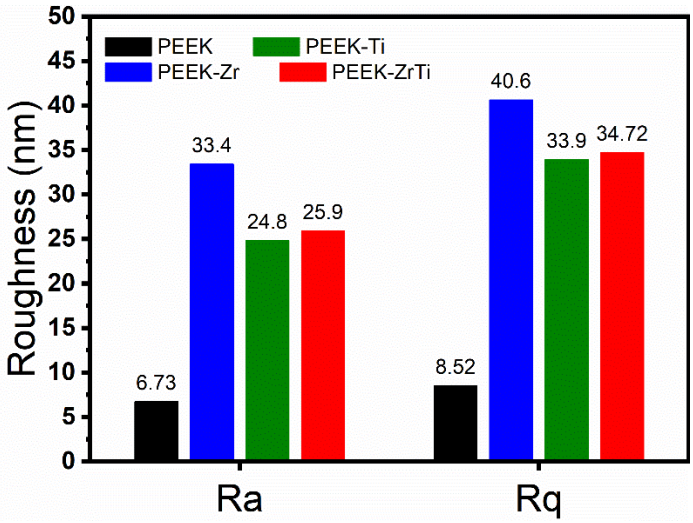

Fig. S10. Surface roughness of PEEK, PEEK-Ti, PEEK-Zr, and PEEK-ZrTi.

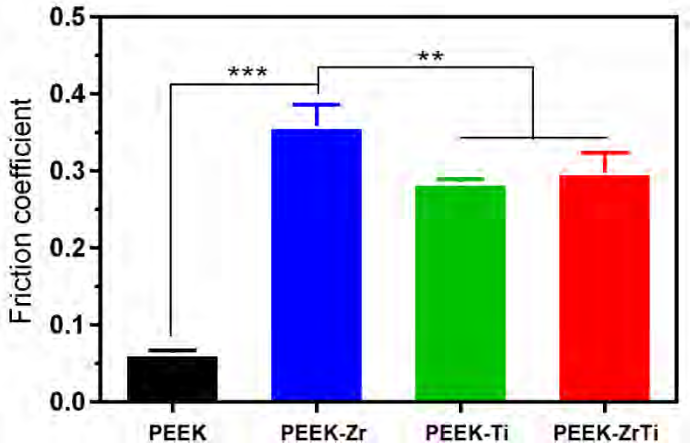

Fig. S11. Surface friction coefficients of PEEK, PEEK-Ti, PEEK-Zr, and PEEK-ZrTi.

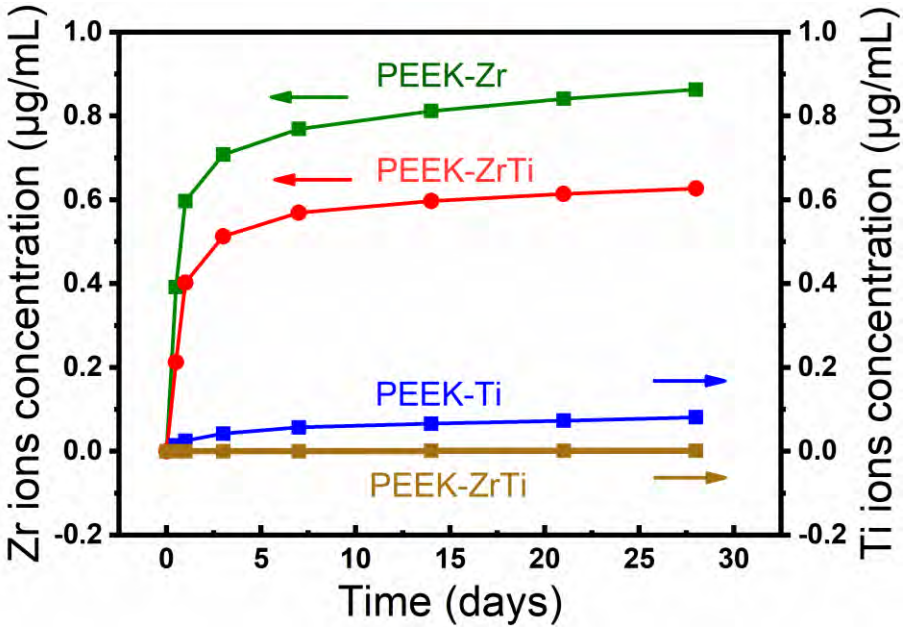

Fig. S12. Cumulative Zr and Ti ions release from PEEK-Zr, PEEK-Ti, and PEEK-ZrTi.

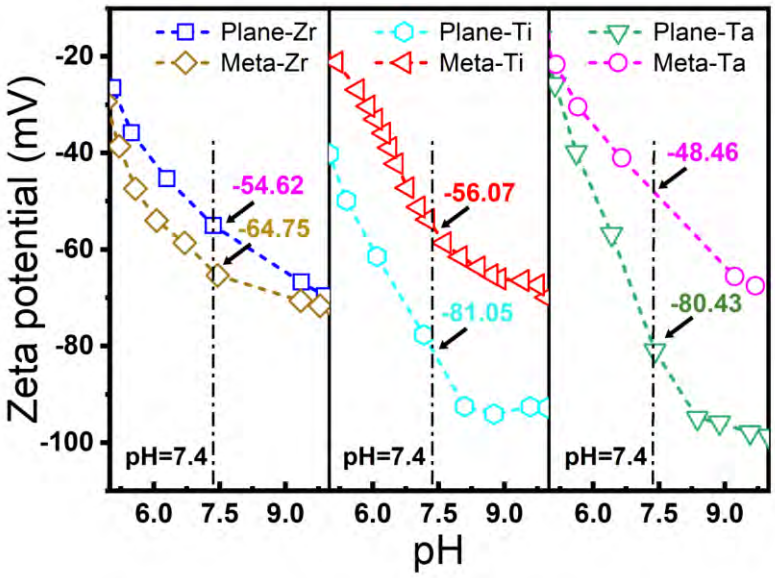

Fig. S13. Surface zeta potential of samples with metasurface (Meta-) and without metasurface (Plane-).

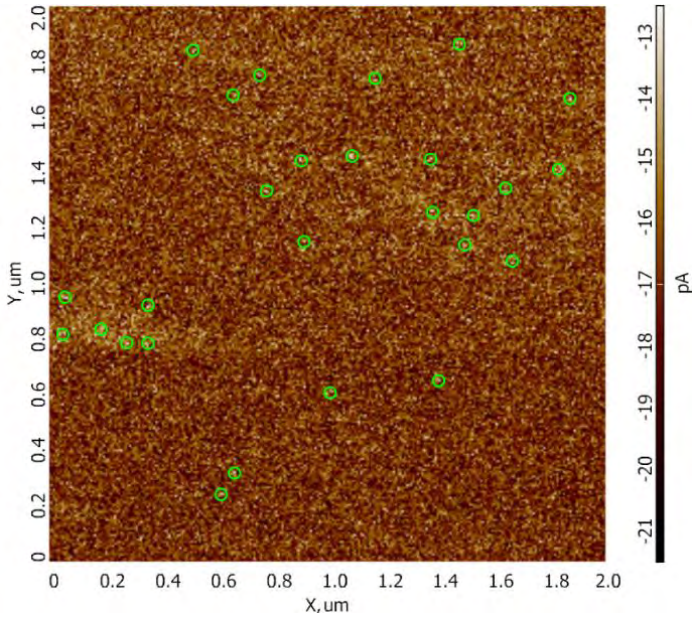

Fig. S14. cAFM image of PEEK-ZrTi.

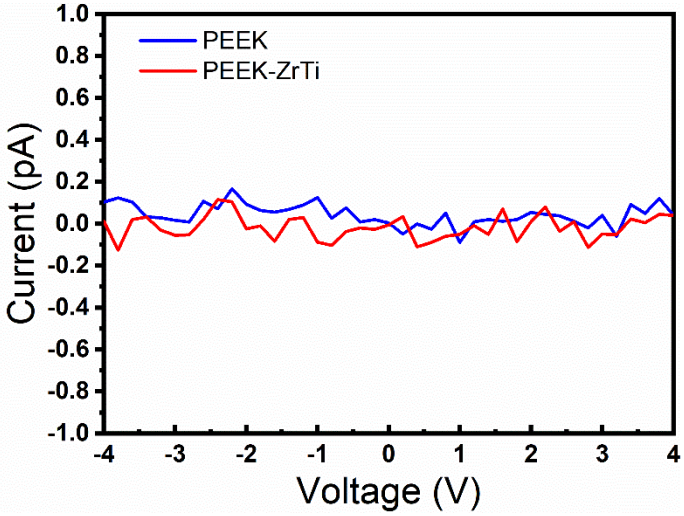

Fig. S15. Surface microregion currents probed by cAFM.

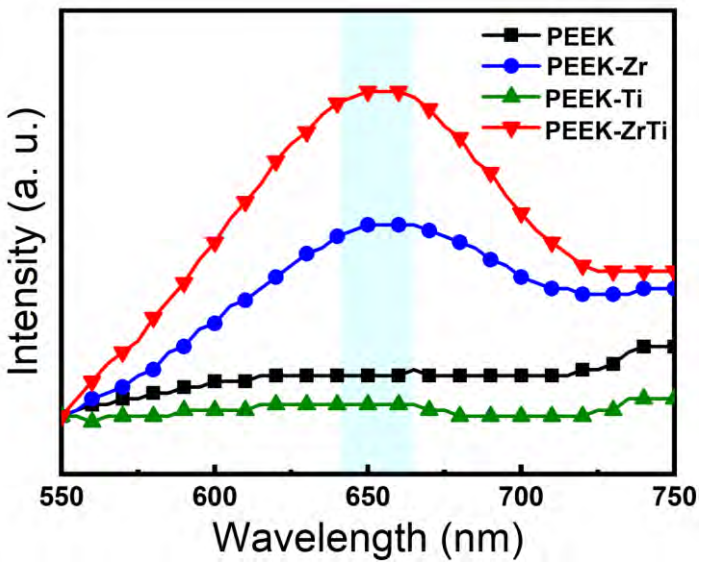

Fig. S16. The galvanic cell effect catalyzes the oxidation of H_2O_2 for TMB color development.

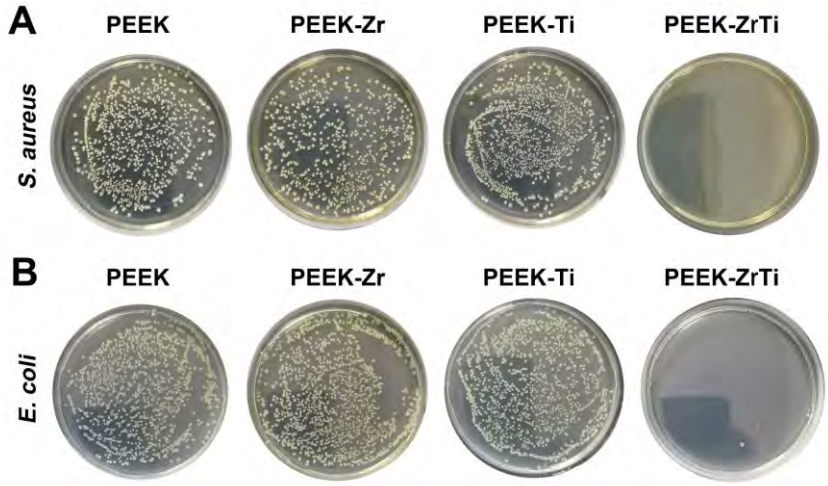

Fig. S17. The photographs of colonies for (A) *S. aureus* and (B) *E. coli*. with various samples.

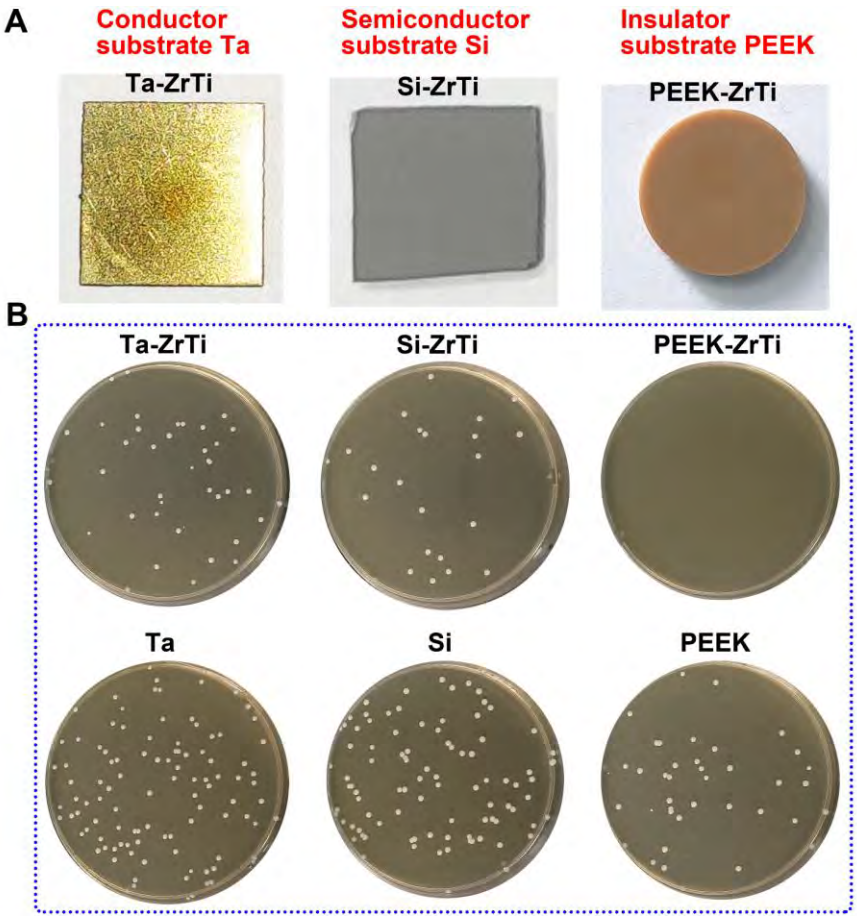

Fig. S18. Photographs of samples (A) and *S. aureus* colonies (B) for Ta-ZrTi, Si-ZrTi, PEEK-ZrTi, Ta, Si, and PEEK.

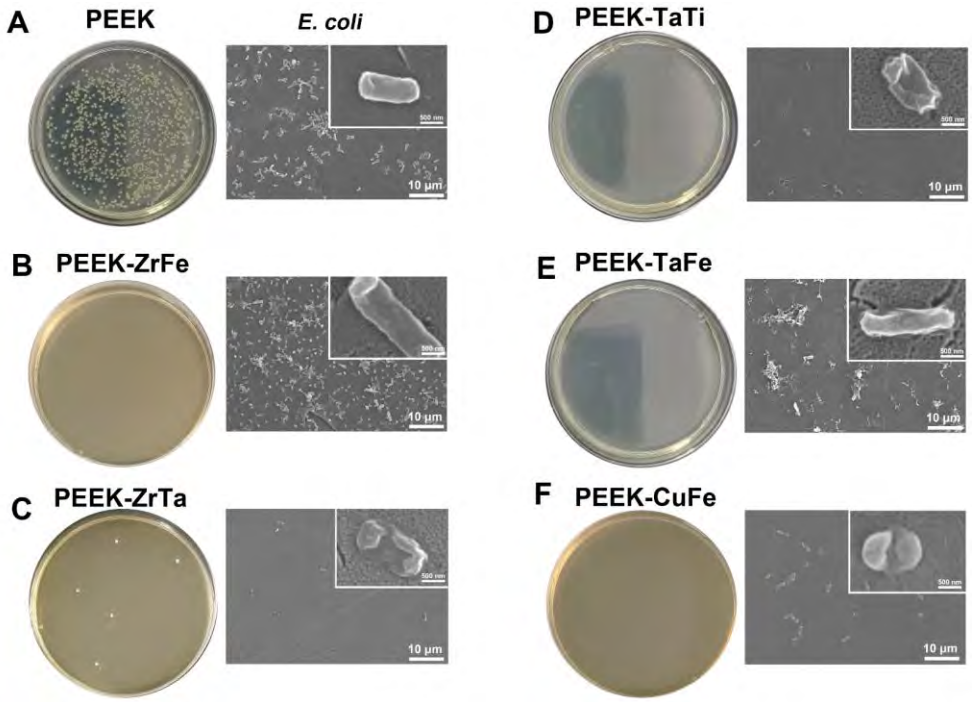

Fig. S19. SEM images and photographs of *S. aureus* colonies for PEEK, PEEK-ZrFe, PEEK-ZrTa, PEEK-TaTi, PEEK-TaFe, and PEEK-CuFe.

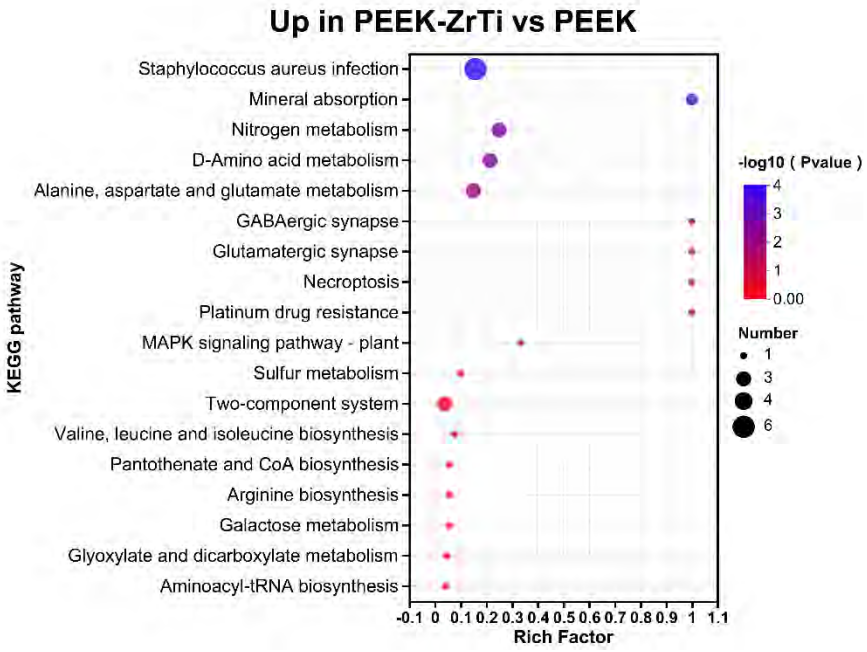

Fig. S20. Up-regulated enriched KEGG pathways analysis of PEEK-ZrTi compared with PEEK.

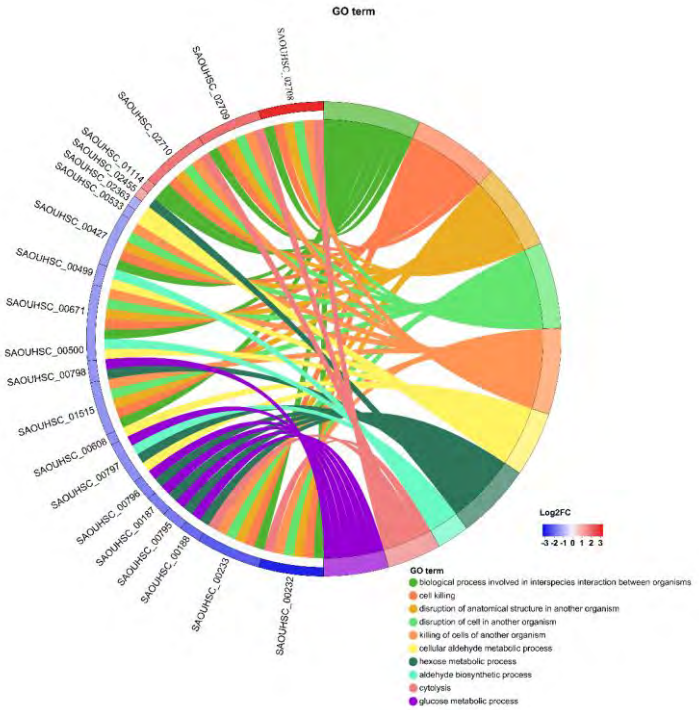

Fig. S21. Chordal diagram on highly expressed gene sequences analyzed from highly regulated GO pathways.

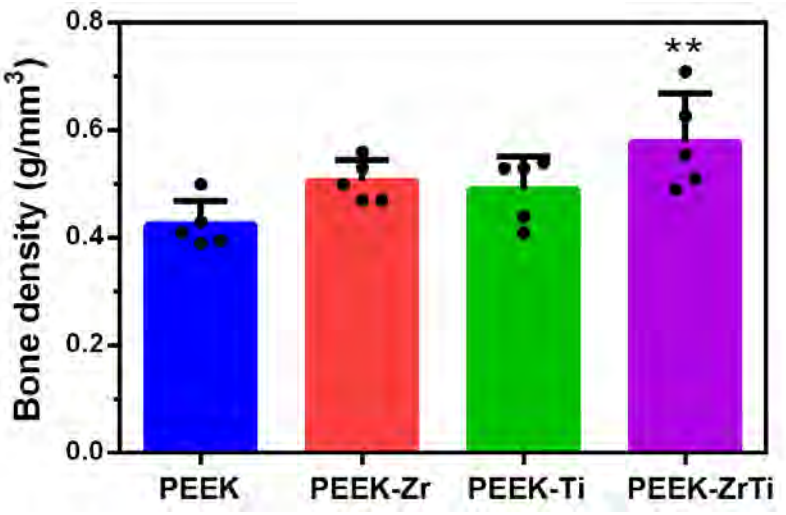

Fig. S22. Quantitative analysis results of bone density of various samples.

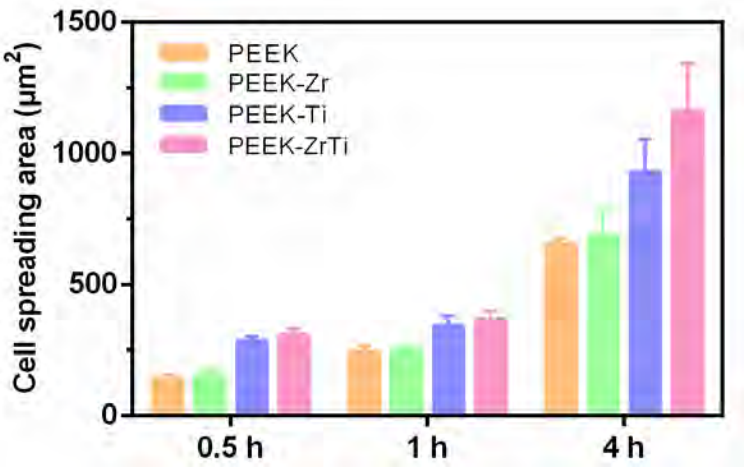

Fig. S23. Analysis statistically of cell spreading area according to cell SEM morphology.

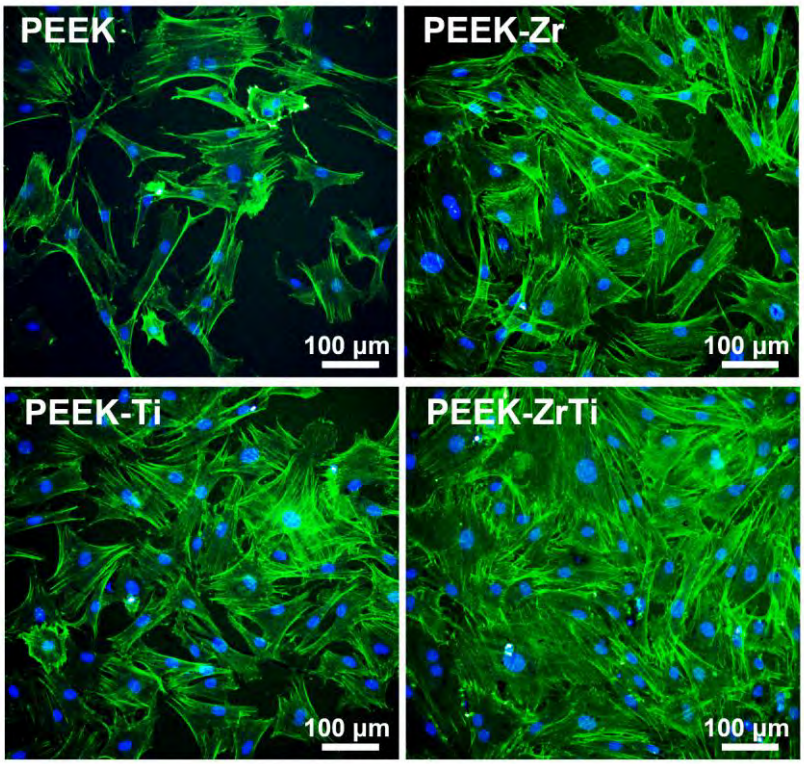

Fig. S24. Fluorescence images of BMSCs cultured with various samples for 12 h.

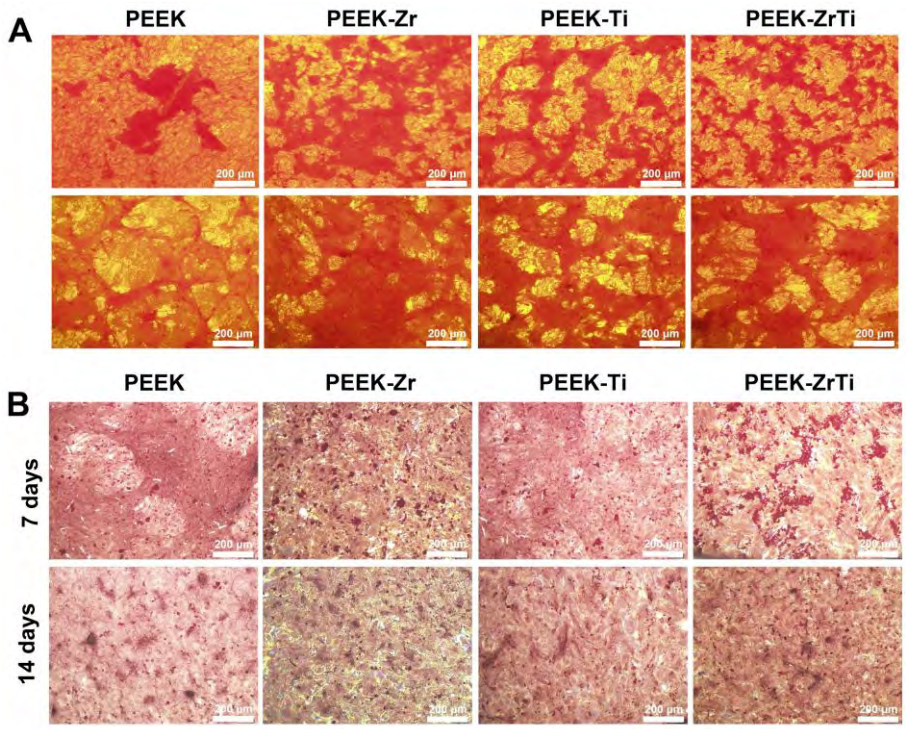

Fig. S25. (A) The result of collagen staining of BMSCs cultured on various samples. (B) The result of extracellular matrix mineralization (ECM) of BMSCs cultured on various samples.

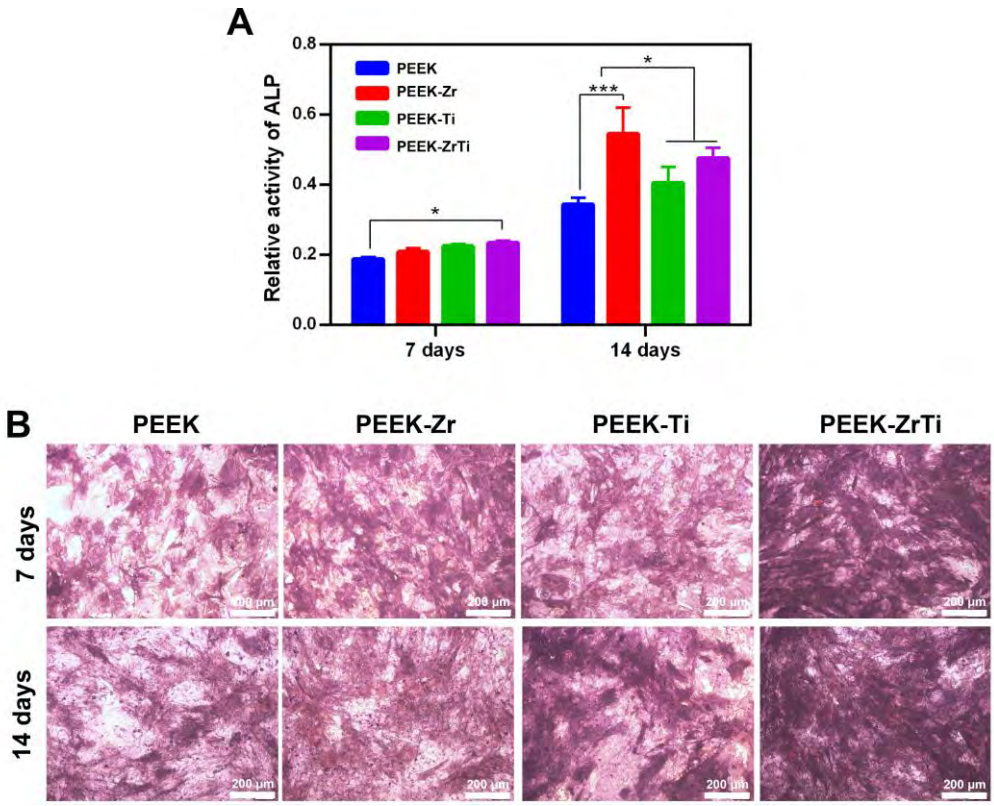

Fig. S26. (A) Quantitative result of ALP activity, and (B) ALP-positive areas of BMSCs cultured on various samples. All the data are expressed as means ± SD (n 0 3) (*p < 0.05, **p < 0.01, and ***p < 0.001).

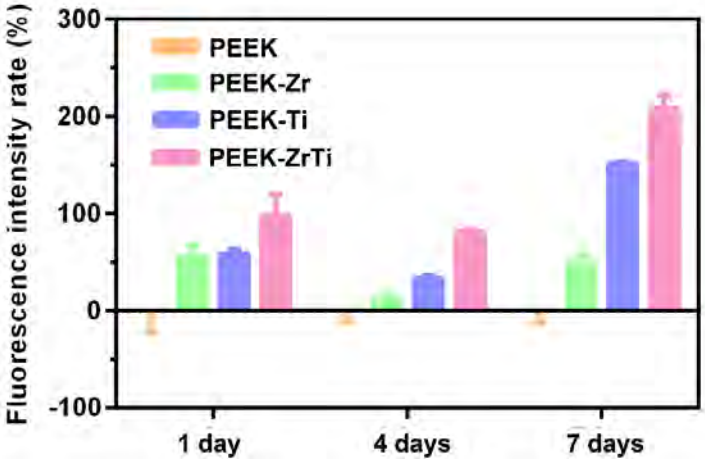

Fig. S27. The cell proliferation rates of PEEK-Zr, PEEK-Ti, and PEEK-ZrTi.

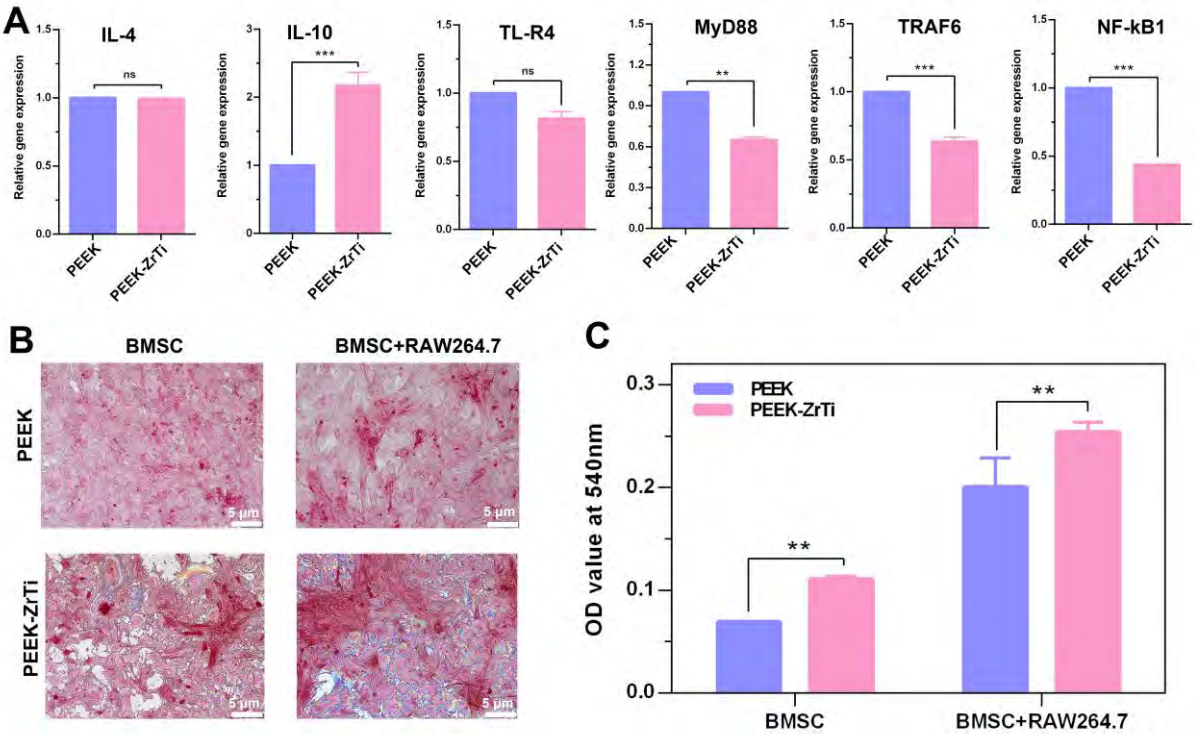

Fig. S28. Inflammation-related behavior of galvanic cell metastructure films. (A) Related gene expression levels of macrophage cultured on various samples for 4 days. Qualitative (B) and quantitative (C) analysis of osteogenic-type mineralization after co-culture of macrophages and BMSC.

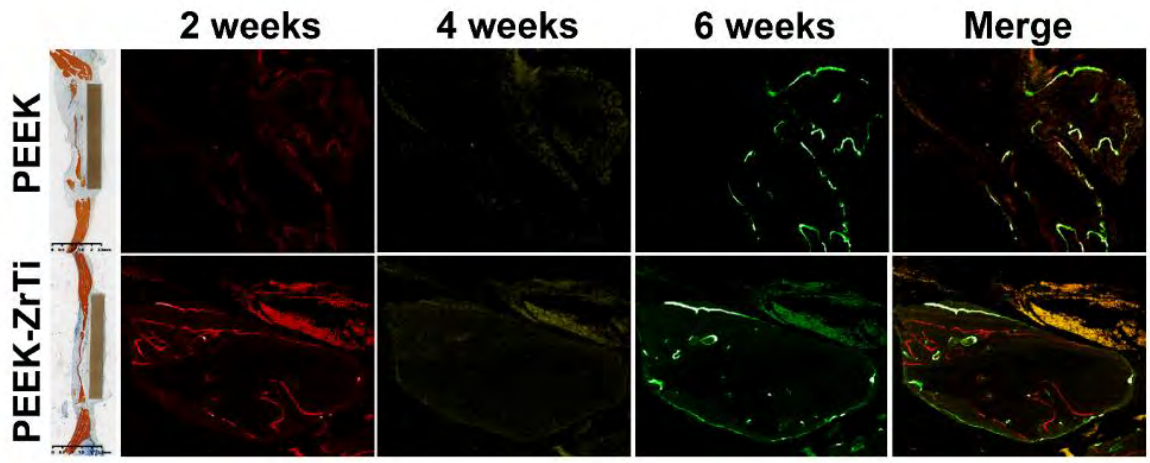

Fig. S29. Van Gieson (VG) staining and sequential fluorescent labeling observations. Red, yellow, and green represent labeling by alizarin red S (2 weeks), tetracycline hydrochloride (4 weeks), and calcein (6 weeks), respectively.

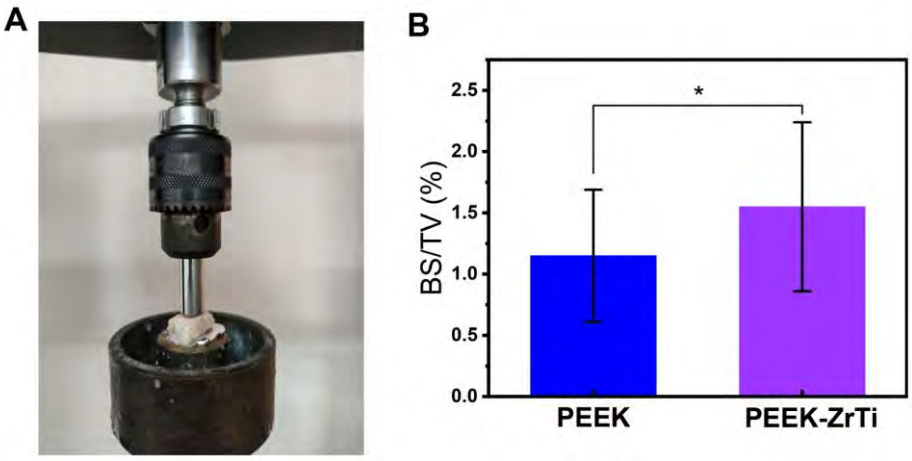

Fig. S30. (A) Torsional force test diagram. (B) Quantitative analysis of bone surface versus tissue volume (BS/TV).

Table S1. Average of RNA-Seq data generated for *S. aureus* samples.

Samples	Raw reads	Clean reads	Unmapped reads	Total mapped (%)
PEEK	21690571	20564871	1125700	94.82
PEEK-ZrTi	21935562	20815403	1120159	94.90

Table S2. Primers associated with osteogenic gene detection.

Gene (mouse)	Primer sequences (F, forward; R, reverse)	Product size (bp)
GAPDH	F: GCT CAG GCC TCT GCG CCC T R: CCT ACT CTC TTG AAT ACC	115
COL-I	F: CTGCCCAGAAGAATATGTATCACC R: GAAGCAAAGTTTCCTCCAAGACC	198
OCN	F: GCCCTGACTGCATTCTGCCTCT R: TCACCACCTTACTGCCCTCCTG	103
ALP	F: CGTCTCCATGGTGGATTATGCT R: CCCAGGCACAGTGGTCAAG	209
BMP-2	F: TGGGTTTGTGGTGGAAGTGGC R: TGGATGTCCTTTACCGTCGTG	154

Table S3. Primers associated with inflammatory gene detection

Gene (mouse)	Primer sequences (F, forward; R, reverse)	Product size (bp)
GAPDH	F: GCT CAG GCC TCT GCG CCC T R: CCT ACT CTC TTG AAT ACC	115
IL-4	F: CCA TGA ATG AGT CCA AGT CC R: TAA CTT ATG AAT TTT TAA T	60
IL-10	F: CCC TTT GCT ATG GTG TCC T R: GTG GCC AGT TTG TTA TTT AT	106
TLR4	F: CAC TAA CGG GAG AAT CCT GTG R: AGG GAC CAT CTT CAT TTC CAT	118
MyD88	F: AGC AGT GTC CCA CAA ACA AAG R: GGC AGT AGC AGA TAA AGG CAT	100
TRAF6	F: ACT GCT GAG TGT TAC TGC CAT R: GCT GTC ATC ATC CAC GAG A	163
NF-κB1	F: TGA CAA GGT TCA GAA AGA TG R: GAA GAC AAT GGC AAA CTG	124

References

[1] T.E. Sheridan, J. Appl. Physiol. 74 (1993) 4903-4906.

[2] L. Gu, M.A. Lieberman, J. Vac. Sci. Technol. A 6 (1988) 2960-2964.

[3] M.A. Lieberman, A.J. Lichtenberg, Principles of Plasma Discharges and Materials Processing, (1970) 2532-2540.

[4] T.E. Sheridan, T.K. Kwok, P.K. Chu, Appl. Phy. Lett. 72 (1998) 1826-1828.

[5] S. Qian, H. Cao, X. Liu, C. Ding, Applied Physics Letters 102 (2013) 243109.